

Signatures of X-rays in the early Universe

Andrei Mesinger^{1*}, Andrea Ferrara¹, & David S. Spiegel²

¹Scuola Normale Superiore, Piazza dei Cavalieri 7, 56126 Pisa, Italy

²Institute for Advanced Study, 1 Einstein Drive Princeton, NJ, 08540, USA

30 October 2012

ABSTRACT

With their long mean free paths and efficient heating of the intergalactic medium (IGM), X-rays could have a dramatic impact on the thermal and ionization history of the Universe. Here we run several semi-numeric simulations of the Dark Ages and the Epoch of Reionization (EoR), including both X-rays and UV radiation fields, attempting to provide an intuitive framework for interpreting upcoming observations. We explore the impact of X-rays on various signals: (i) *Reionization history*: including X-rays results in an earlier, slightly more extended EoR. However, efficient thermal feedback from X-ray heating could yield an extended epoch in which the Universe was $\approx 10\%$ ionized. (ii) *Reionization morphology*: a sizable ($\sim 10\%$) contribution of X-rays to reionization results in a more uniform morphology, though the impact is modest when compared at the same global neutral fraction, \bar{x}_{HI} . Specifically, X-rays produce a dearth of fully neutral regions and a suppression of small-scale ($k \gtrsim 0.1 \text{Mpc}^{-1}$) ionization power by a factor of $\lesssim 2$. However, these changes in morphology cannot be countered by increasing the bias of the ionizing sources, making them a robust indicator of an X-ray contribution to the EoR. (iii) *The kinetic Sunyaev-Zel'dovich (kSZ) effect*: at a fixed reionization history, X-rays decrease the kSZ power at $l = 3000$ by $\approx 0.5 \mu\text{K}^2$. Our extreme model in which X-rays entirely drive reionization is the only one which is marginally consistent with the recent upper limits on this signal from the South Pole Telescope, assuming no thermal Sunyaev-Zel'dovich (tSZ) – dusty galaxy cross-correlation. Since this extreme model is unlikely, we conclude that there should be a sizable tSZ-dusty galaxy cross-correlation. (iv) *The redshifted 21cm signal*: the impact of X-rays on the 21cm power spectrum during the advanced stages of reionization ($\bar{x}_{\text{HI}} \lesssim 0.8$) is modest, except in extreme, X-ray dominated models. The largest impact of X-rays is to govern the timing and duration of IGM heating. In fact, unless thermal feedback is efficient, the epoch of X-ray heating likely overlaps with the beginning of reionization ($\bar{x}_{\text{HI}} \gtrsim 0.9$). This results in a 21cm power spectrum which is ~ 10 – 100 times higher than obtained from naive estimates ignoring this overlap. On the other hand, if thermal feedback is efficient, the resulting extended epoch between X-ray heating and reionization could provide a clean probe of the matter power spectrum in emission, at redshifts more accessible than the Dark Ages.

Key words: cosmology: theory – intergalactic medium – early Universe – reionization – dark ages – X-rays:galaxies

1 INTRODUCTION

Cosmic reionization is the last global baryonic phase change, and acts as powerful probe of early Universe physics and the first generations of galaxies. Although the details remain unclear, it is generally accepted that reionization is mostly driven by stellar sources inside dwarf galaxies that accrete gas via molecular or atomic hydrogen line cooling. The relatively soft ultraviolet (UV) spectra of such stellar sources results in a reionization which is “inside-out” on large scales: ionized bubbles grow around the first, highly clustered sources, with their eventual coalescence signaling the completion

of reionization (e.g. Furlanetto et al. 2004; McQuinn et al. 2007; Trac & Cen 2007; Zahn et al. 2011). Such UV-driven reionization scenarios result in a very inhomogeneous ionization field, where the large-scale clustering of galaxies determines the ionization morphology.

On the other hand, reionization would be noticeably different if it were driven by higher energy, X-ray photons. Firstly, reionization morphology would be more uniform, due to the relatively large mean free path for X-rays (e.g. McQuinn 2012):

$$\lambda_X \approx 20 \bar{x}_{\text{HI}}^{-1} \left(\frac{E_X}{300 \text{eV}} \right)^{2.6} \left(\frac{1+z}{10} \right)^{-2} \text{cMpc}, \quad (1)$$

Here \bar{x}_{HI} is the mean neutral fraction of the intergalactic medium

* email: andrei.mesinger@sns.it

(IGM) and E_X is the photon energy. Secondly, most of the X-ray energy gets deposited as heat when \bar{x}_{HI} surpasses a few percent (e.g. Shull & van Steenberg 1985; Furlanetto & Stoever 2010; Valdés et al. 2010), quickly raising the Jeans mass in the IGM. Therefore, if X-rays were abundant in the early Universe, thermal feedback might delay the end stages of reionization (e.g. Ricotti & Ostriker 2004; Kuhlen & Madau 2005). Such a scenario could accommodate a relatively large optical depth to Thompson scattering (Komatsu et al. 2011) and still allow stellar UV emission to complete reionization at $z \sim 6\text{--}7$, consistent with recent observations (e.g. Bolton et al. 2011; Dijkstra et al. 2011; Pentericci et al. 2011; Schroeder et al. 2012).¹

Several observations indirectly limit the allowed contribution of X-rays to reionization. Firstly, the number density of bright active galactic nuclei (AGN) decreases sharply towards high redshifts (e.g. Madau et al. 1999; Fan et al. 2001). Although faint AGN (so-called miniquasars) could still contribute (e.g. Madau et al. 2004; Volonteri & Gnedin 2009), the parameter space for such models is decreasing with more sensitive surveys probing further down the AGN luminosity function (e.g. Willott et al. 2010). Attention has also focused on other sources of X-rays, such as high-mass X-ray binaries (HMXBs), which dominate the X-ray contribution of star-forming galaxies (e.g. Mineo et al. 2012). The strongest constraints on X-ray reionization comes from the present-day unresolved X-ray background (XRB). The XRB is an indirect probe, since the observed photons originating from high-redshifts are energetic enough to have mean free paths greater than the Hubble length. Therefore the observed photons are not the ones interacting with the IGM. Nevertheless, estimates of the unresolved XRB from the Chandra deep fields (CDFs; Hickox & Markevitch 2007) rule out reionization models driven by hard X-ray spectra (with photon energy indices $\alpha \lesssim 1$; Dijkstra et al. 2004; McQuinn 2012), provided there is no spectral break towards high-energies ($E_X \gtrsim 10$ keV).

Despite the limited parameter space, there has recently been a resurgence of interest in X-ray reionization. This has been motivated by several factors.

(i) The observed population of high-redshift galaxies ($z \sim 6\text{--}10$) seem unable to maintain an ionized Universe, barring an evolution in galaxy properties (for example, an increase with redshift in the fraction of ionizing photons capable of making it out of the galaxy; e.g. Mitra et al. 2012; Kuhlen & Faucher-Giguere 2012; Fontanot et al. 2012).

(ii) The observed anti-correlation of HMXBs with metallicity (e.g. Crowther et al. 2010; Kaaret et al. 2011), as well as theoretical studies proposing a high binary fraction among the first stars (Turk et al. 2009; Stacy et al. 2010), motivate a higher contribution from HMXBs in early galaxies (Mirabel et al. 2011)².

(iii) The recent upper limit on the kinetic Sunyaev-Zel'dovich (kSZ) signal from the South Pole Telescope (SPT)³ by Reichardt

¹ However, similar extended reionization scenarios could result without X-rays: for example from strong, self-regulating feedback on small galaxies (e.g. Springel & Hernquist 2003; Ahn et al. 2012; Pawlik et al. 2012) and/or from reionization “stalling” when the HII regions grow to surpass the attenuation length of ionizing UV photons (Furlanetto & Mesinger 2009; Crociani et al. 2011; Alvarez & Abel 2012).

² Note however that there is no evidence of such an evolution of the X-ray luminosity to star formation rate (SFR) ratio, up to $z \sim 6$ (Cowie et al. 2012). This $z \sim 6$ constraint is however strongly dependent on the assumed SFR and X-ray spectral index.

³ <http://pole.uchicago.edu/>

et al. (2012) is inconsistent with stellar-driven UV reionization models (Mesinger et al. 2012), unless there is a non-negligible correlation in the thermal SZ – cosmic infrared background (CIB) signal. This measurement is a probe of the ionization structure on ~ 20 Mpc scales; X-rays with long mean free paths are a natural candidate for erasing such structure (Visbal & Loeb 2011; Mesinger et al. 2012).

(iv) Cappelluti et al. (2012) recently detected a correlation between the CIB and the soft XRB. The observed cross-power is best explained if the sources are at high redshifts ($z \gtrsim 7$).

In this work, we do not attempt to predict whether or not X-rays are important to reionization (see, e.g. Dijkstra et al. 2004; Srbinovsky & Wyithe 2007; Volonteri & Gnedin 2009; McQuinn 2012). Instead we explore various observational signatures of X-rays in the reionization and pre-ionization epochs. We attempt to provide an intuitive framework for interpreting upcoming observations. Given the many astrophysical uncertainties, we adopt a parametric approach, looking for general trends and physical insight.

We model X-rays in the early Universe using a public code, 21CMFAST. This is a “semi-numerical” simulation, using well-tested and efficient algorithms to compute various cosmic fields. Due to their long mean free paths, very large boxes (several hundred comoving Mpc) are required in order to properly model X-rays (as well as the photons responsible for pumping the 21cm line; see below). Computing these radiation fields for the dominant galaxy population in the early Universe is computationally impractical for conventional radiative transfer (RT) algorithms. On the other hand, analytic approaches do not preserve the spatial structure we are investigating. Therefore semi-numerical simulations are uniquely suited for this task.

This paper is organized as follows. In §2, we present our simulations. In §3 we discuss our results, including the impact of early X-rays on the evolution of the global reionization signal (§3.1), reionization morphology (§3.2), the kSZ signal (§3.3), and the redshifted 21cm signal (§3.4). Finally, in §4, we summarize our conclusions.

Except for fluxes, we quote all quantities in comoving units. We adopt the background cosmological parameters (Ω_Λ , Ω_M , Ω_b , n , σ_8 , H_0) = (0.73, 0.27, 0.046, 0.96, 0.82, 70 km s⁻¹ Mpc⁻¹), consistent with the seven-year results of the *WMAP* satellite (WMAP7; Komatsu et al. 2011).

2 SIMULATIONS

We use a parallelized version of the publicly available 21CMFAST code⁴. This code uses perturbation theory (PT) to generate the density and velocity fields, and PT plus the excursion-set formalism of Furlanetto et al. (2004) to generate the ionization fields. We summarize these calculations below. For further details on these algorithms, see Mesinger & Furlanetto (2007), Zahn et al. (2011) and Mesinger et al. (2011).

2.1 Ionization and heating by X-ray photons

In the early stages of reionization, there is a small HII region local to each source (e.g. Cen 2006), whereas the X-rays are able to penetrate deep into the mostly-neutral IGM. Outside of the local HII regions, we compute the temperature, T_K , and ionized fraction, x_e ,

⁴ <http://homepage.sns.it/mesinger/Sim.html>

at a given redshift, z , and position in our simulation box, \mathbf{x} , according to:

$$\frac{dx_e(\mathbf{x}, z)}{dz} = \frac{dt}{dz} [\Gamma_{\text{ion}} - \alpha_A C x_e^2 n_b f_H] , \quad (2)$$

$$\begin{aligned} \frac{dT_K(\mathbf{x}, z)}{dz} = & \frac{2}{3k_B(1+x_e)} \frac{dt}{dz} \sum_p \epsilon_p \\ & + \frac{2T_K}{3n_b} \frac{dn_b}{dz} - \frac{T_K}{1+x_e} \frac{dx_e}{dz} , \end{aligned} \quad (3)$$

where $n_b = \bar{n}_{b,0}(1+z)^3[1+\delta_{\text{nl}}(\mathbf{x}, z)]$ is the total (H + He) baryonic number density at (\mathbf{x}, z) , $\epsilon_p(\mathbf{x}, z)$ is the heating rate per baryon for process p in erg s^{-1} , Γ_{ion} is the ionization rate per baryon, α_A is the case-A recombination coefficient, $C \equiv \langle n^2 \rangle / \langle n \rangle^2$ is the clumping factor on the scale of the simulation cell (here taken to be $C = 2$), k_B is the Boltzmann constant, f_H is the hydrogen number fraction.

For X-ray heating and ionization, we have:

$$\epsilon_X(\mathbf{x}, z) = \int_{\text{Max}[\nu_0, \nu_{\tau=1}]}^{\infty} d\nu \frac{4\pi J}{h\nu} \sum_i (h\nu - E_i^{\text{th}}) f_{\text{heat}} f_i x_i \sigma_i \quad (4)$$

and

$$\Gamma_{\text{ion}}(\mathbf{x}, z) = \int_{\text{Max}[\nu_0, \nu_{\tau=1}]}^{\infty} d\nu \frac{4\pi J}{h\nu} \sum_i f_i x_i \sigma_i F_i , \quad (5)$$

$$F_i = (h\nu - E_i^{\text{th}}) \left(\frac{f_{\text{ion,HI}}}{E_{\text{HI}}^{\text{th}}} + \frac{f_{\text{ion,HeI}}}{E_{\text{HeI}}^{\text{th}}} + \frac{f_{\text{ion,HeII}}}{E_{\text{HeII}}^{\text{th}}} \right) + 1$$

where the frequency integral includes the contribution from photons within a mean free path of $(\mathbf{x}, z)^5$, and we perform a sum over species, $i = \text{HI, HeI, or HeII}$, in which f_i is the number fraction, x_i is the cell's species ionization fraction [which for HI and HeI is $(1 - x_e)$, and for HeII is x_e], σ_i the ionization cross-section, and E_i^{th} is the ionization threshold energy of species i . Furthermore, $f_{\text{heat}}[h\nu - E_i^{\text{th}}, x_e(\mathbf{x}, z)]$ and $f_{\text{ion,j}}[h\nu - E_i^{\text{th}}, x_e(\mathbf{x}, z), j]$ are the fraction of the primary electron's energy going into heat and secondary ionizations of species j respectively (taken from Furlanetto & Stoever 2010).

In the above equations, the angle-averaged specific intensity, $J(\nu, \mathbf{x}, z)$, (in $\text{erg s}^{-1} \text{Hz}^{-1} \text{cm}^{-2} \text{sr}^{-1}$) can be computed integrating along the light-cone:

$$J(\nu, \mathbf{x}, z) = \frac{(1+z)^3}{4\pi} \int_z^{\infty} dz' \frac{cdt}{dz'} \epsilon_{h\nu} , \quad (6)$$

and the comoving specific emissivity is evaluated at $\nu_e = \nu(1+z')/(1+z)$:

$$\begin{aligned} \epsilon_{h\nu}(\nu_e, \mathbf{x}, z') = & \alpha h \frac{N_X}{\mu m_p} \left(\frac{\nu_e}{\nu_0} \right)^{-\alpha} \\ & \left[\rho_{\text{crit},0} \Omega_b f_* (1 + \bar{\delta}_{\text{nl}}) \frac{df_{\text{coll}}}{dt} \right] , \end{aligned} \quad (7)$$

⁵ Note that this spatially-averaged, frequency-dependent opacity is computed including the total ionized fraction from both X-rays and UV photons (see Mesinger et al. 2011).

where N_X is the number of X-ray photons per stellar baryon, μm_p is the mean baryon mass, $\rho_{\text{crit},0}$ is the current critical density, f_* is fraction of baryons converted into stars (we take $f_* = 0.1$), $\bar{\delta}_{\text{nl}}$ is the mean non-linear overdensity and f_{coll} is the fraction of matter collapsed into halos with virial temperatures greater than T_{vir} , which is computed according to the hybrid prescription of Barkana & Loeb (2008). The quantity in the brackets is the comoving star formation rate density (SFRD). The specific emissivity is chosen to have a spectral (energy) index of $\alpha = 1.5$ both in order to facilitate comparisons with previous works (e.g. Pritchard & Furlanetto 2007; Santos et al. 2008; Baek et al. 2010; Mesinger et al. 2011), and also since a significant contribution from harder spectra is ruled out by observations of the XRB (McQuinn 2012) unless there is a break at high energies ($E_X \gtrsim 10 \text{ keV}$).

2.2 Ionization by UV photons

The contribution of UV photons to reionization is computed as a post-processing step, following the X-rays. We use the excursion-set prescription of Furlanetto et al. (2004), slightly modified according to Zahn et al. (2011) (our 'FFRT' scheme). This algorithm determines whether a region is ionized by comparing the (integrated) number of ionizing photons to the number of neutral atoms. Specifically, a simulation cell at coordinate \mathbf{x} is flagged as ionized if

$$\zeta_{\text{UV}} f_{\text{coll}}(\mathbf{x}, z, R) \geq 1 - x_e(\mathbf{x}, z, R) , \quad (8)$$

where ζ_{UV} is an ionizing efficiency parameter (described below), and as above, f_{coll} is the fraction of mass residing in dark matter halos inside a sphere of radius R and mass $M = 4/3\pi R^3 \rho$, where $\rho = \bar{\rho}[1 + \bar{\delta}_{\text{nl}}]$. In this work we include on the RHS the mean fraction of neutral hydrogen remaining within R : $1 - x_e$, computed according to eq. (2).

As for the X-rays, this tabulation includes all halos above a set virial temperature threshold, T_{vir} . We do not explicitly compute individual halo locations (as in Mesinger & Furlanetto 2007), but instead apply the conditional excursion-set formalism directly on the non-linear density field to compute f_{coll} (Zahn et al. 2011). The ionization field is also computed following the excursion-set approach (e.g., Bond et al. 1991; Lacey & Cole 1993; Furlanetto et al. 2004). We decrease the filter scale R , starting from some maximum value R_{max} . A physical choice for R_{max} corresponds to the mean free path of ionizing photons, R_{mfp} (Furlanetto & Oh 2005; Choudhury et al. 2009; Alvarez & Abel 2012). We take $R_{\text{max}} = 40 \text{ Mpc}$, consistent with recent observations (e.g. Songaila & Cowie 2010) and theoretical estimates (e.g. McQuinn et al. 2011). If at any R the criterion in equation (8) is met, this cell is flagged as ionized.

Note that this formalism assumes that UV photons, with their short mean free paths, carve out fully-ionized HII regions in the IGM (e.g. Zahn et al. 2011). If we denote the covering factor of these HII regions as Q_{HII} , then the total ionized fraction (including the partial ionizations from X-rays in eq. 2), can be written as $\bar{x}_i \approx Q_{\text{HII}} + (1 - Q_{\text{HII}})x_e$. Similarly, we denote the mean neutral fraction as $\bar{x}_{\text{HI}} = 1 - \bar{x}_i$.

2.3 The runs

Our simulation boxes are 750 Mpc on a side, with a resolution of 500^3 . We integrate the evolution from $z = 40$ down to $z = 5.6$, including the end of the Dark Ages and reionization. Here we discuss

the astrophysical parameters we vary, and motivate some fiducial choices.

We parameterize the ionizing efficiency of UV photons as follows:

$$f_{\text{UV}} \equiv \frac{\zeta_{\text{UV}}}{30} \approx \left(\frac{N_{\gamma}}{4400} \right) \left(\frac{f_{\text{esc}}}{0.1} \right) \left(\frac{f_*}{0.1} \right) \left(\frac{1.5}{1 + \bar{n}_{\text{rec}}} \right), \quad (9)$$

where f_{esc} is the fraction of UV ionizing photons that escape into the IGM, N_{γ} is the number of ionizing photons per stellar baryon, and \bar{n}_{rec} is the mean number of recombinations per baryon (a factor which appears since ζ_{UV} is defined after integrating the ionization rate over cosmic time). A value of $f_{\text{UV}} \approx 1$ agrees with the observed value of $\tau_e \approx 0.09$ (Komatsu et al. 2011), in the absence of an X-ray contribution to reionization. Although our models depend only on the product in eq. (9), we show on the RHS some reasonable values for the component terms. $N_{\gamma} = 4400$ is expected for PopII stars (e.g. Barkana & Loeb 2005), and studies of the high-redshift Lyman alpha forest suggest $\bar{n}_{\text{rec}} \sim 0$ (Miralda-Escudé 2003; Bolton & Haehnelt 2007; McQuinn et al. 2011). On the other hand, the parameters f_{esc} and f_* are extremely uncertain in high-redshift galaxies (e.g. Gnedin et al. 2008; Wise & Cen 2009; Ferrara & Loeb 2012), though their product might be more robust (Wise & Cen 2009; Paardekooper et al. 2011).

Similarly, the X-ray efficiency is parameterized as follows:

$$f_X \equiv \left(\frac{N_X}{0.4} \right) \left(\frac{f_*}{0.1} \right). \quad (10)$$

The value of $N_X = 0.4$ X-ray photons per stellar baryon corresponds to a total X-ray luminosity above $h\nu_0 = 0.3$ keV of $L_{X,0.3+\text{keV}} \approx 10^{40} \text{ erg s}^{-1} (M_{\odot} \text{ yr}^{-1})^{-1}$, using our spectral energy index of $\alpha = 1.5$. This choice is consistent with (a factor of ≈ 1.8 higher than) an extrapolation from the 0.5–8 keV measurement of Mineo et al. (2012), $L_{X,0.5-8\text{keV}} \approx 3 \times 10^{39} \text{ erg s}^{-1} (M_{\odot} \text{ yr}^{-1})^{-1}$. Mineo et al. (2012) find a factor of 2–3 intrinsic scatter in this relation for their sample of star-forming galaxies, while other studies in different bands have estimates which are also within a factor of few of this value (e.g. Gilfanov et al. 2004; Ranalli et al. 2003; Persic et al. 2004; Persic & Rephaeli 2007; Lehmer et al. 2010)⁶. Recently, the 4 Ms exposure of the Chandra Deep Field-South (CDF-S; e.g. Xue et al. 2011) has allowed us to study the redshift evolution of this relation. There is some evidence of a (weak) evolution (Basu-Zych et al. 2012; though see Cowie et al. 2012). However, interpreting the derived upper limits on the X-ray flux of $z \sim 6$ galaxies is very uncertain, and in particular is heavily dependent on the assumed extrapolation to the soft X-rays which are the ones actually interacting with the IGM. For example, the 2σ upper limits from Cowie et al. (2012) still allow $N_X \sim 1000$ for their $z \sim 6$ galaxy sample, e.g. assuming a SFR of $0.1 M_{\odot} \text{ yr}^{-1}$, $h\nu_0 = 0.3$ keV and $\alpha = 1.5$.

The strongest constraint on the X-ray contribution to reionization comes from the unresolved soft XRB observed in the CDFs. As mentioned in the introduction, the XRB is an indirect probe since the observed photons are not the ones interacting with the IGM.

⁶ We note that our fiducial choice ($f_X = 1$) for the X-ray efficiency, N_X , is a factor of ≈ 4 lower than that used in prior studies, based on an extrapolation of the earlier 2–10keV measurement by Gilfanov et al. (2004) down to $h\nu_0 = 0.2$ keV. Therefore our $f_X = 5$ model below is a closer match to most prior theoretical studies (e.g. Furlanetto 2006; Pritchard & Furlanetto 2007; Santos et al. 2008; Warszawski et al. 2009; Mack & Wyithe 2011)

Therefore, constraints are sensitive to the assumed spectral index or any spectral break at high energies. Hickox & Markevitch (2007) estimate the 1–2 keV unresolved XRB to be $3.4 \pm 1.4 \times 10^{-13} \text{ erg s}^{-1} \text{ cm}^{-2} \text{ deg}^{-2}$. This can be compared with the XRB at $z = 0$ in our models, estimated from eq. (6). X-rays in our fiducial model below make a negligible contribution to the XRB, contributing 0.4% (5%) of the unresolved XRB if the sources remain on until $z \approx 10$ (6). On the other hand, in our $f_X = 10^4$ “extreme” model where X-rays dominate reionization (see below), the sources at $z \gtrsim 10$ already saturate the unresolved XRB. This is roughly consistent with recent simple estimates (c.f. Fig. 1 in McQuinn 2012; see also Dijkstra et al. 2004; Salvaterra et al. 2007).

Following previous works (e.g. Furlanetto 2006; Pritchard & Furlanetto 2007; Santos et al. 2008; Warszawski et al. 2009; Baek et al. 2010; Mesinger et al. 2011), we assume a simple obscuration model for our X-ray sources, with a step function at $h\nu_0$. This allows us to separately treat the sources of X-ray and UV photons, isolating the imprint of the former. On the other hand, the stellar-driven UV is assumed to be soft enough that each photon above the Lyman limit produces a single ionization (eq. 8). Although sources of X-rays in principle do also contribute some UV photons, local observations find that the majority of both AGN and HMXBs are significantly obscured (e.g. Lutovinov et al. 2005; Tozzi et al. 2006). Photons below our fiducial choice of $h\nu_0 = 300$ eV have optical depths exceeding unity for $N_{\text{HI}} \gtrsim 10^{21.5} \text{ cm}^{-2}$, consistent with the column densities seen in high-redshift gamma-ray bursts (GRBs) (Totani et al. 2006; Greiner et al. 2009).

The final free parameter we vary is T_{vir} , the minimum virial temperature of halos hosting galaxies. Although our formalism allows for disparate values of T_{vir} for X-ray and UV sources, for simplicity we use the same value for both populations. Our fiducial choice of $T_{\text{vir}} = 10^4$ K corresponds to the atomic cooling threshold. Although the first stars are likely hosted by smaller halos with $T_{\text{vir}} \sim \text{few} \times 10^3$ K (e.g. Haiman et al. 1996; Abel et al. 2002; Bromm et al. 2002), star formation inside such small halos was likely inefficient (with a handful of stars per halo), and was likely suppressed by heating and feedback processes (Haiman et al. 2000; Ricotti et al. 2001; Mesinger et al. 2006; Haiman & Bryan 2006; Tseliakhovich & Hirata 2010; O’Leary & McQuinn 2012). We therefore do not include radiation from such so-called minihalos. T_{vir} could also have been larger than 10^4 K: radiative and/or mechanical feedback (e.g. Springel & Hernquist 2003) eventually suppresses star formation inside $T_{\text{vir}} \lesssim 10^5$ K halos, though the details and timing of these processes are not well understood at high redshifts (e.g. Mesinger & Dijkstra 2008; Okamoto et al. 2008; Pawlik & Schaye 2009)⁷.

In summary, the total (integrated) number of photons per stellar baryon escaping into the IGM in our models is given by $N_{\gamma} f_{\text{esc}}$ for the ionizing UV photons, and N_X for the X-rays. For the UV we don’t specifically adopt a spectral energy distribution (SED), instead assuming that the spectra are soft enough that the majority of photons will ionize at most one atom. For the X-rays, we assume a rest-frame luminosity, $L_e \propto \nu^{1.5}$, extending from $\nu = \nu_0$ to $\nu = \infty$.

⁷ It is unlikely that T_{vir} is much greater than $\text{few} \times 10^5$ K, since these values approximately correspond to the faint end of the observed galaxy luminosity functions at $z \sim 6$ (e.g. Bouwens et al. 2008; Labbe et al. 2010; Salvaterra et al. 2011; Finlator et al. 2011). Additionally, high T_{vir} models have difficulty in latching onto the slow evolution of the observed emissivity, as inferred from the Ly α forest at $3 < z < 6$ (see Fig. 12 in Mesinger et al. 2012).

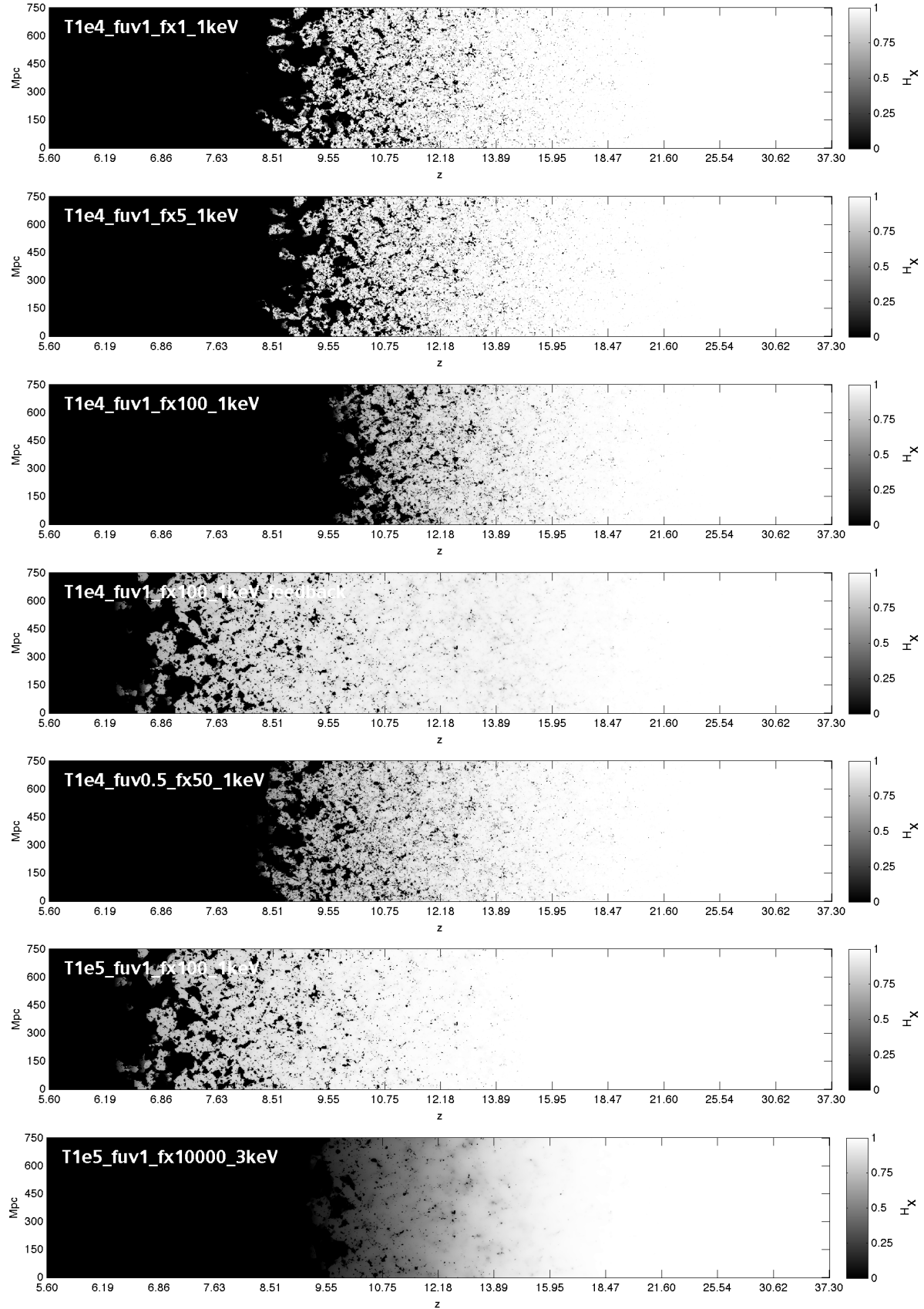


Figure 1. Slices through ionization fields, showing evolution with comoving distance along the light cone (x-axis). All slices are 1.5 Mpc (1 cell) deep.

Run name	$T_{\text{vir}} (10^4 \text{ K})$	f_{UV}	f_X	$h\nu_0 (\text{keV})$	τ_e	X-ray fraction	$[\Delta_{i3000}^{\text{patchy}}]^2 (\mu\text{K}^2)$
T1e4_fuv1_fx1_1keV	1	1	1	0.3	0.092	3%	2.3
T1e4_fuv1_fx5_1keV	1	1	5	0.3	0.094	8%	2.3
T1e4_fuv1_fx100_1keV	1	1	100	0.3	0.107	46%	2.1
T1e4_fuv1_fx100_1keV_feedback	1 → 10	1	100	0.3	0.069	46%	1.3
T1e4_fuv0.5_fx50_1keV	1	0.5	50	0.3	0.092	45%	1.8
T1e5_fuv1_fx100_1keV	10	1	100	0.3	0.063	48%	1.2
T1e5_fuv1_fx10000_3keV	10	1	10^4	0.9	0.108	96%	0.95

Table 1. Model parameters and related observational signatures, as described in the text.

We list all of our runs below (summarized also in Table 1):

- **T1e4_fuv1_fx1_1keV** – This is our “fiducial” run, with $T_{\text{vir}} = 10^4 \text{ K}$, $f_{\text{UV}} = 1$, $f_X = 1$, and $h\nu_0 = 0.3 \text{ keV}$, resulting in a spectrally-averaged mean photon energy $h\bar{\nu} = 0.9 \text{ keV}$. This model predicts $\tau_e = 0.092^8$, consistent with WMAP7. In this fiducial case, UV photons dominate reionization, with X-rays accounting for only $\approx 3\%$ of the total ionizations.

- **T1e4_fuv1_fx5_1keV** – This run differs from the fiducial only in having an X-ray efficiency which is a factor of ≈ 5 higher, making it more in line with several previous works (e.g. Furlanetto 2006; Pritchard & Furlanetto 2007; Santos et al. 2008; Warszawski et al. 2009; Mack & Wyithe 2011; Valdés et al. 2012).

- **T1e4_fuv1_fx100_1keV** – Here we increase the X-ray efficiency by a factor of 100 from our fiducial choice. In this model, X-rays ionize approximately half of the IGM⁹. We use this model as a reference scenario in which X-rays are important, and vary additional parameters below.

- **T1e4_fuv1_fx100_1keV_feedback** – This model is the same as T1e4_fuv1_fx100_1keV but includes a simple, extreme prescription for thermal feedback, with T_{vir} increasing to 10^5 K , when the mean temperature of the IGM surpasses 10^4 K . Although thermal (i.e. radiative feedback) was initially suspected of being important (e.g. Shapiro et al. 1994; Thoul & Weinberg 1996; Gnedin 2000), later studies concluded that its impact was

⁸ Interestingly, the fact that reionization is “inside-out” on large scales results in a different τ_e then would be estimated assuming homogeneous reionization. This is due to the fact that τ_e is proportional to the sightline-averaged integral of the ionized fraction times the density: $\langle x_i \times n \rangle$, and $\langle x_i \times n \rangle \neq \langle x_i \rangle \times \langle n \rangle$. In patchy reionization models, where the high-redshift overdensities hosting early galaxies ionize first, this inequality results in values of τ_e that are a few percent higher than estimated assuming x_i and n are uncorrelated (e.g. $\tau_e = 0.092$ instead of $\tau_e = 0.088$ in our fiducial model). Understandably, this bias decreases as reionization becomes more homogeneous, such that in our “extreme” model τ_e has the same value, 0.11, computed both ways. The correlation of the ionization and density fields can have a $\lesssim 10\%$ effect on other global signals, such as the 21cm brightness temperature during the advanced stages of reionization (Wheeler et al., in preparation). We therefore stress that the correlations between various cosmic fields should be taken into account for precise estimates of even globally-averaged signals.

⁹ The relative contribution of UV and X-ray photons to reionization can also be estimated from their relative number of ionizations per stellar baryon: $N_\gamma f_{\text{esc}}$ for the UV, and $N_X N_i$ for the X-rays. Here N_i is the mean number of ionizations per X-ray photon. Depending on the spectrum and ionized fraction, secondary ionizations can drive $N_i \approx 10\text{--}20$ early in reionization, transitioning to $N_i = 1$ late in reionization when all of the primary electron’s energy gets deposited as heat. Using $N_i \approx 10$ and the parameter values in our T1e4_fuv1_fx100_1keV model, we confirm that the number of ionizations by X-rays and UV photons are comparable: $N_X N_i \sim 400 \sim N_\gamma f_{\text{esc}}$.

smaller at high-redshifts (e.g. Ricotti et al. 2002; Kuhlen & Madau 2005; Mesinger & Dijkstra 2008; Okamoto et al. 2008). Since the T1e4_fuv1_fx100_1keV_feedback model is extreme in that it includes an *instantaneous* transition to a *high* T_{vir} value, it serves to bracket the expected effects of feedback.

- **T1e4_fuv0.5_fx50_1keV** – X-rays also contribute about 1/2 of the ionizations in this model, but the efficiencies of both the UV and X-rays have been lowered by a factor of ≈ 0.52 . This is done in order to delay reionization so that τ_e is the same as in our fiducial run, facilitating comparison.

- **T1e5_fuv1_fx100_1keV** – This model has $f_X = 100$ as in T1e4_fuv1_fx100_1keV, but with $T_{\text{vir}} = 10^5 \text{ K}$ throughout cosmic time, corresponding to inefficient star formation in smaller dwarf galaxies.

- **T1e5_fuv1_fx10000_3keV** – This is our “extreme” model, in which high energy X-rays drive reionization (accounting for over 96% of all ionizations). Specifically, we take $f_X = 10^4$, $T_{\text{vir}} = 10^5 \text{ K}$, and $h\nu_0 = 0.9 \text{ keV}$ (requiring $N_{\text{HI}} \gtrsim 10^{23} \text{ cm}^{-2}$, and resulting in a spectrally-averaged photon energy of $h\bar{\nu} = 2.7 \text{ keV}$). As mentioned above, the unresolved XRB is saturated by $z \gtrsim 10$ in this model.

3 RESULTS

3.1 Evolution and Timing of Reionization

In Fig. 1, we show slices through ionization fields, showing evolution with comoving line-of-sight (LOS) distance along the light cone (x-axis). X-rays have a negligible contribution to reionization in the fiducial model. The morphology remains unaffected as the X-ray efficiency, f_X , is increased by a factor of five. However, as the X-ray efficiency is increased further, one starts to notice several differences in timing and morphology. As expected, reionization occurs earlier, has less small-scale structure, with a partially-ionized homogeneous “haze” developing in the early stages of reionization. We quantify these trends below.

In the top panel of Fig. 2 we plot the reionization histories of our runs. Again, there is little change from the fiducial model (*black solid curve*) as the X-ray efficiency is increased by a factor of ≈ 5 (*dotted red curve*). However, increasing the X-ray efficiency by a factor of 100 (*orange short-dashed curve*) causes reionization to happen earlier, with the midpoint shifting by $\Delta z \approx 1$.

Increasing the contribution of X-rays to reionization also causes reionization to happen more gradually, as can be seen when comparing the blue dot-short dashed and black solid curves, which are normalized to have the same τ_e (c.f. the top and fifth panels in Fig. 1). This effect is most seen in the extreme case of T1e5_fuv1_fx10000_3keV, where reionization is dominated by X-rays. In this case, $d\bar{x}_{\text{HI}}/dz$ is roughly constant after $\bar{x}_{\text{HI}} \lesssim 0.8$, and

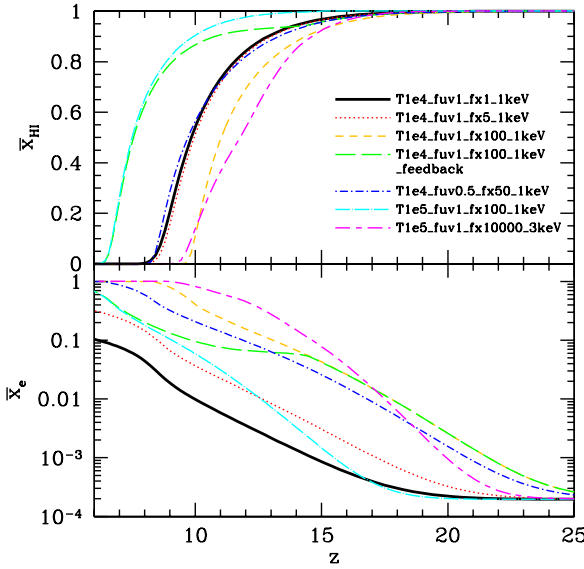


Figure 2. Top panel: Reionization histories of the runs listed in Table 1. Bottom panel: The mean ionization fraction, \bar{x}_e , generated only by X-ray ionizations (ignoring the UV contribution except to compute the IGM opacity to X-rays).

the reionization history doesn't show the “knee” feature where the slope increases in the middle stages as the collapse fraction grows. This is due to the fact that as X-ray driven reionization progresses, the increasing abundance of galaxies is countered by the decreasing efficiency of X-ray ionization: $f_{\text{ion,j}} \rightarrow 0$ as $\bar{x}_{\text{HI}} \rightarrow 0$, so only primary ionizations from X-ray photons can complete reionization (e.g. Shull & van Steenberg 1985; Furlanetto & Stoever 2010; Valdés et al. 2010).

Aside from directly ionizing the IGM, the heat input from early X-rays can result in thermal feedback: raising the effective Jeans mass required for gas to efficiently accrete onto DM halos (see the discussion in §2.3). If this process is important, the first generations of galaxies would sterilize themselves, and reionization would be delayed until more massive DM halos emerge (see the fourth panel in Fig. 1). The extreme limit of this scenario is explored in T1e4_fuv1_fx100_1keV_feedback (green long dashed curve), and results in a reionization history with a tail of $\bar{x}_{\text{HI}} \approx 90\%$ extending to high- z , as also noted by Ricotti & Ostriker (2004).

In the bottom panel of Fig. 2, we show the mean ionization fraction generated only by X-ray ionizations (i.e. ignoring the contribution from UV photons). In fiducial reionization scenarios driven by UV ionizations, x_e corresponds to the electron fraction in the “neutral” IGM, outside of the almost fully-ionized HII regions local to the sources. As \bar{x}_{HI} decreases, the resulting increase in the X-ray “horizon” (see eq. 1) is the likely cause of the slight steepening of dx_e/dz (note that the filling factor of HII regions, Q_{HII} , is still used to estimate the opacity of the IGM when computing the X-ray flux Mesinger et al. 2011). Baek et al. (2010) also noted that such a redshifting X-ray background can have a non-negligible contribution to X-ray driven reionization. This effect is most evident in the models where $T_{\text{vir}} \sim 10^4$ K halos drive reionization; on the other hand, more massive sources on the exponential tail of the mass function appear too suddenly to show this feature (e.g. Lidz et al. 2007).

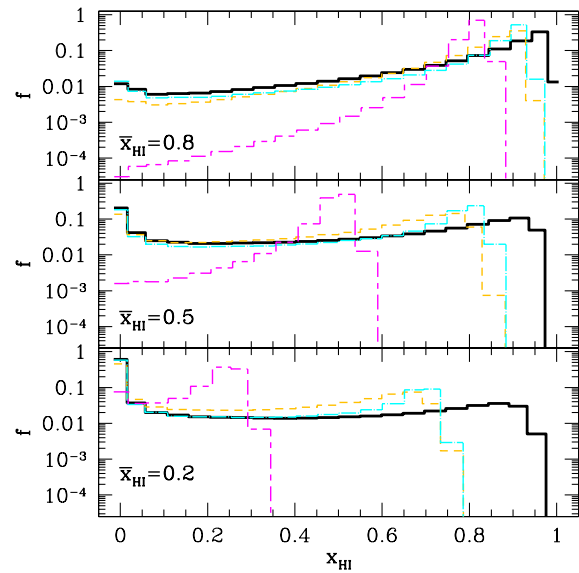


Figure 3. Fraction of $R_{\text{filter}} = 3$ Mpc regions having a given x_{HI} . All smoothing is done with a top-hat filter. The runs are denoted by the same line styles as in Fig. 2: T1e4_fuv1_fx1_1keV (black solid), T1e4_fuv1_fx100_1keV (orange short-dashed), T1e5_fuv1_fx100_1keV (cyan dot long-dashed), T1e5_fuv1_fx10000_3keV (magenta short long dashed). The panels correspond to $\bar{x}_{\text{HI}} = 0.8, 0.5, 0.2$ (top to bottom).

3.2 Ionization Morphology

It has been suggested that abundant X-rays in the early Universe could have a large impact on reionization morphology (e.g., see the discussion in Haiman 2011). From Fig. 1, we can see that this is the case only in extreme models, with no “soft” ($\lesssim 1$ keV) X-rays. In this section we further quantify the impact of X-rays on reionization morphology.

In Fig. 3, we plot the histograms of the neutral fraction in $R_{\text{filter}} = 3$ Mpc regions, at different stages of reionization. The fiducial run (black solid curve) results in the most inhomogeneous ionization field since it has the smallest contribution of X-rays.

As the X-ray efficiency is increased by a factor of 100 (orange short-dashed curve), the ionization field becomes noticeably more homogeneous. There is a significant suppression (a factor of ≈ 3) in the number of fully ionized regions in the early stages ($\bar{x}_{\text{HI}} \approx 0.8$). At a fixed global neutral fraction, \bar{x}_{HI} , including X-rays decreases the relative contribution of fully-ionized HII regions (driven mostly by UV sources). Furthermore, the histogram becomes noticeably more peaked with a sharp reduction in the number of highly-neutral regions. Specifically, there are no 3 Mpc regions having $x_{\text{HI}} \gtrsim 0.95, 0.85, 0.75$ at $\bar{x}_{\text{HI}} \approx 0.8, 0.5, 0.2$, respectively.

As sources are hosted by rarer, more biased halos, the reionization field becomes slightly more inhomogeneous (compare the orange and cyan curves). However, this difference is not as large as the one imprinted by X-ray reionization, since the DM halo bias increases only by several tens of percent going from $T_{\text{vir}} = 10^4$ K to $T_{\text{vir}} = 10^5$ K (McQuinn et al. 2007). *This result indicates that a significant contribution (\sim tens of percent) of X-rays to reionization results in a more homogeneous reionization morphology which cannot be countered by having more biased sources.*

The magenta curve in Fig. 3 corresponds to the “extreme” model, T1e5_fuv1_fx10000_3keV, in which X-rays complete reionization. The sources in this model also have an SED with a more energetic mean photon energy of $h\bar{\nu} \approx 3$ keV. As could be guessed

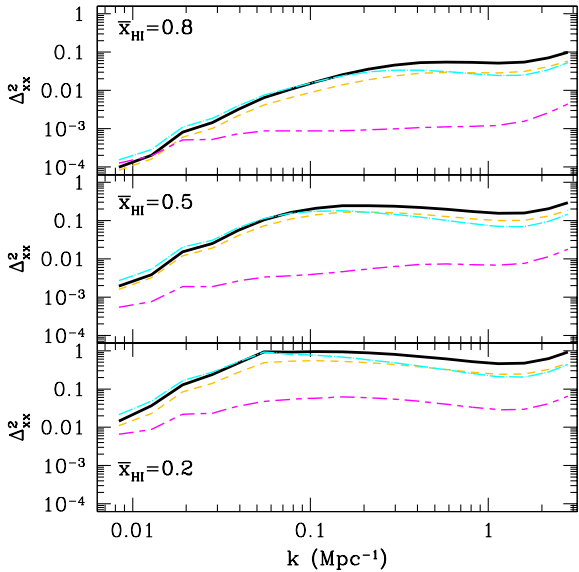


Figure 4. Power spectra of the ionization fields for the same models and epochs shown in Fig. 3.

from Fig. 1, the reionization morphology in this model is significantly more homogeneous, with the ionization histograms sharply peaked around \bar{x}_{HI} .

In Fig. 4 we plot the ionization field power spectra ($\Delta_{\text{xx}}^2 = k^3/(2\pi^2 V) \langle |\delta_{\text{xx}}|^2 \rangle_k$, with $\delta_{\text{xx}} = x_{\text{HI}}/\bar{x}_{\text{HI}} - 1$) for the same models and epochs shown in Fig. 3. The same trends discussed above can also be seen in this figure. The fiducial model displays the standard ‘‘knee’’ feature, which shifts to larger scales imprinting the HII region size in the early stages of reionization, and either the matter power spectrum or the mean free path of UV photons (set by Lyman limit systems) in the late stages of reionization (e.g. Alvarez & Abel 2012). This ‘‘knee’’ feature should be one of the fundamental observables of the upcoming 21cm interferometry measurements.

Increasing the X-ray contribution to reionization to $\sim 50\%$ (comparing the orange and black curves) results in a roughly scale-free suppression of the power spectrum by a factor of $\lesssim 2$. However the ‘‘knee’’ feature is still preserved. Further moving the sources to more biased halos (comparing the orange and blue curves) results in a more peaked bubble distribution, with a suppression of small-scale power and a boost in large-scale power. We note that *the small-scale power is most sensitive to the X-rays, while the large scale power is most sensitive to the halos which host the sources* (e.g. McQuinn et al. 2007). On the other hand, the extreme model with X-ray driven reionization results in a very large (1–2 orders of magnitude) suppression of power, especially on small-scales.

These trends are qualitatively evident in Fig. 5, where we show slices through the ionization fields at $\bar{x}_{\text{HI}} = 0.9$. The first panel shows just ionizations from X-rays in the T1e4_fuv0.5_fx50_1keV model (turning off the UV sources). The second panel shows just the ionizations resulting from UV photons in the same model (turning off the X-ray sources). It is evident that X-rays result in a smoother ionization field. However, even without any UV sources, the soft X-rays are able to carve out highly ionized regions surrounding the first, most highly biased sources.

The third panel shows the total ionization field in the same model, resulting from both X-ray and UV sources (note that this field is not just the sum of the first two, but instead corresponds to an earlier epoch since all panels are chosen at $\bar{x}_{\text{HI}} \approx 0.9$). We see that small ionization structures are most affected by X-rays,

as also noted in Fig. 4. When compared at the same \bar{x}_{HI} , the ionizations contributing to the small, late appearing, UV-driven HII regions, effectively shift to the uniform, partially ionized, X-ray driven ‘‘haze’’. Larger HII regions are less affected, since these correspond to highly-biased regions hosting the first X-ray sources. In these regions the X-rays themselves pre-ionized a large fraction of the HI, making it easier for the UV photons to finish the job.

The fourth panel corresponds to the T1e5_fuv1_fx10000_3keV model. Unlike the model shown in the first panel, the T1e5_fuv1_fx10000_3keV model contains no soft X-rays with energies below 0.9 keV. The higher energy photons in this extreme model understandably create a more uniform ionization field.

3.3 The kinetic Sunyaev-Zel'dovich signal from inhomogeneous reionization

One of the most promising near-term probes of reionization is the kSZ signal. The kSZ results from the scattering of cosmic microwave background (CMB) photons off of inhomogeneities in the ionization and velocity fields (Sunyaev & Zeldovich 1980; Ostriker & Vishniac 1986; Vishniac 1987; Ma & Fry 2002). The kSZ can be decomposed into the post-reionization, so-called Ostriker-Vishniac (OV; Ostriker & Vishniac 1986; Ma & Fry 2002) component, and a component from during reionization referred to as the patchy kSZ (Gruzinov & Hu 1998; Knox et al. 1998). Observational efforts with the Atacama Cosmology Telescope (ACT) and the South Pole Telescope (SPT) are poised to detect this signal for the first time, with projected $1 \mu\text{K}^2$ -level sensitivity to the dimensionless kSZ power spectrum around a multipole of $l = 3000$, $[\Delta_{l=3000}]^2$. $l = 3000$ is the ‘‘sweet-spot’’, corresponding to scales small enough not to be dominated by the primary anisotropies and large enough not to be dominated by the CIB. As an integral measurement, $[\Delta_{l=3000}]^2$ is sensitive to the duration of the epoch during which ionized structures were of comparable size ($l = 3000$ corresponds to $\approx 20 \text{ Mpc}$ at high- z).

Indeed, recent SPT measurements place a bound of $[\Delta_{l=3000}]^2 < 2.8 \mu\text{K}^2$ at 95% confidence limit (C.L.), which degrades to $[\Delta_{l=3000}]^2 < 6 \mu\text{K}^2$ if a significant correlation between the tSZ and the CIB is allowed (Reichardt et al. 2012). Mesinger et al. (2012) showed that the $[\Delta_{l=3000}]^2 < 2.8 \mu\text{K}^2$ constraint is *inconsistent with all physically-motivated, UV-driven reionization scenarios, even with conservatively low estimates of the OV contribution*. Reionization by UV photons is simply too inhomogeneous on $\approx 20 \text{ Mpc}$ scales to accommodate this constraint, with the patchy kSZ signal contributing at least $1.5 \mu\text{K}^2$.

This implies that either: (i) there is a significant correlation between the CIB and the tSZ; and/or (ii) the early stages of reionization occurred in a much more homogeneous manner, perhaps driven by X-ray photons with large mean free paths. Upcoming combined analyses of microwave and Herschel far infrared data will likely test the former scenario. Here we explore the latter.

The patchy kSZ signal can be decreased by: (i) lowering the redshift of reionization; (ii) shortening its duration; and/or (iii) decreasing ionization structure on $l = 3000$ scales¹⁰. X-ray driven reionization does the latter.

In Fig. 6 we plot the kSZ angular power spectrum $C_l^{\text{kSZ}} \equiv$

¹⁰ Note that a measurement of the patchy kSZ power combined with τ_e does *not* uniquely determine the redshift and duration of reionization, since the ionization morphology affects the shape of the kSZ power, in addition to its amplitude (Mesinger et al. 2012).

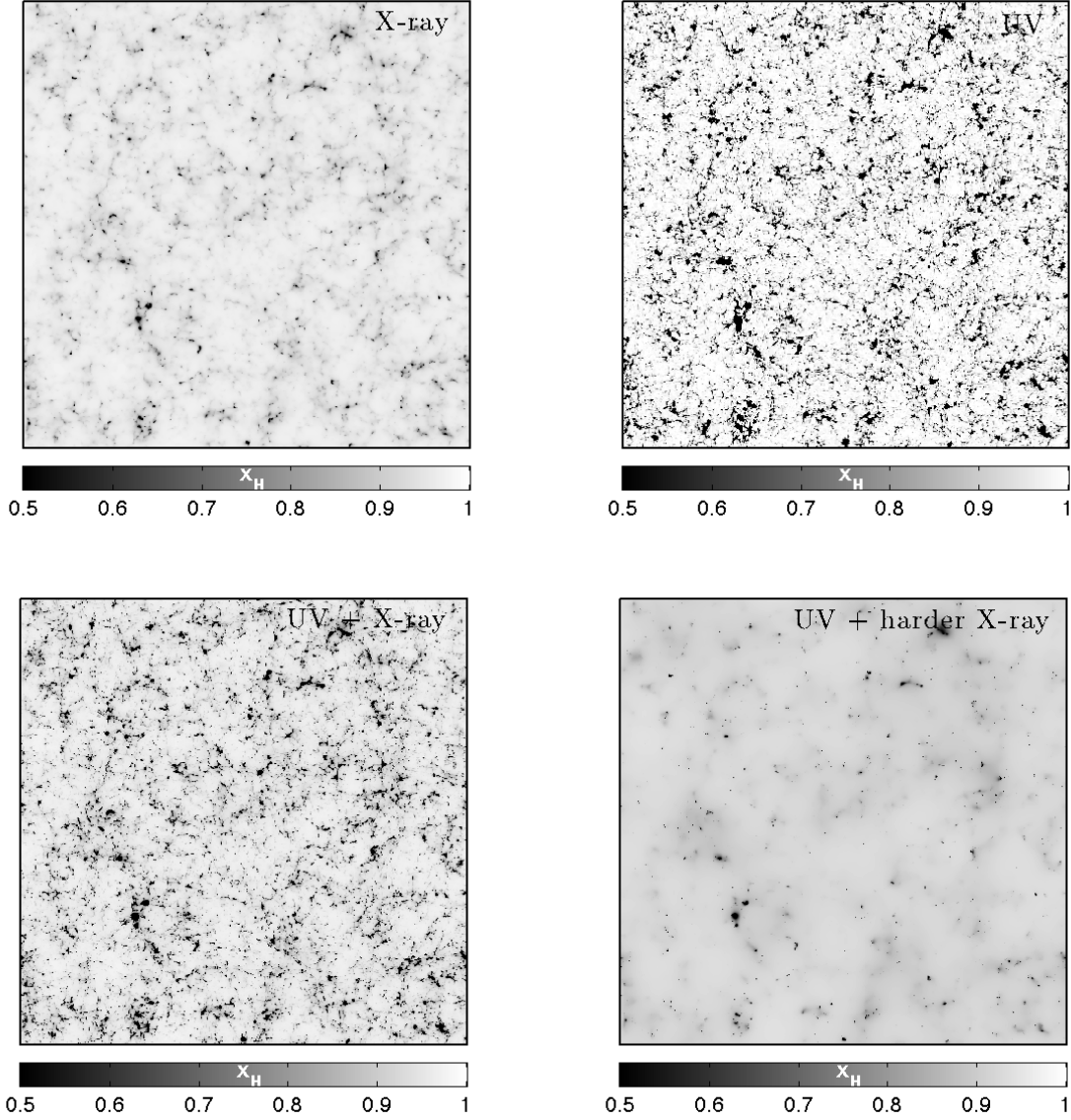


Figure 5. Slices through ionization fields at $\bar{x}_{\text{HI}} = 0.9$. The first panel shows just X-ray ionizations in the T1e4_fuv0.5_fx50_1keV model (i.e. $1-x_e$ computed with eq. 2). The second panel corresponds to ionizations from UV photons in the same model, but without any X-ray sources. The third panel is the total ionization field in the T1e4_fuv0.5_fx50_1keV model. The last panel is the ionization field in the T1e5_fuv1_fx10000_3keV run, where soft X-rays below $\lesssim 0.9$ keV are obscured. All slices are 1.5 Mpc deep, and show only the $0.5 < \bar{x}_{\text{HI}} < 1$ range for improved contrast.

$T_{\text{cmb}}^2 |\tilde{\delta}_T(k)|^2$, where $T_{\text{cmb}} = 2.73$ K and $\tilde{\delta}_T$ is the Fourier transform of

$$\delta_T \equiv \frac{\Delta T}{T}(\hat{\mathbf{u}}) = \sigma_T \int dz c(dt/dz) e^{-\tau_e(z)} n_e \hat{\mathbf{u}} \cdot \mathbf{v}, \quad (11)$$

and $\hat{\mathbf{u}}$ is the LOS unit vector, σ_T is the Thomson scattering cross section, $\tau_e(z)$ is the Thomson optical depth to redshift z in the direction $\hat{\mathbf{u}}$, $\mathbf{v}(\hat{\mathbf{u}}, z)$ is the peculiar velocity, and $n_e(\hat{\mathbf{u}}, z)$ is the electron number density. Following Mesinger et al. (2012), we only show the power sourced from $z > 5.6$, corresponding roughly to the lower limit on the end of reionization (McGreer et al. 2011). Power spectrum values at $l = 3000$ from our models are also shown in Table 1. The fiducial model has $l = 3000$ kSZ power from $z > 5.6$ of $2.3 \mu\text{K}^2$.

Interestingly, we see that X-rays have only a modest impact on the shape of the power spectrum at $l \gtrsim 1000$, unless they dominate

reionization (magenta curve). This is in line with what we saw in the previous section: the effects on the morphology at fixed \bar{x}_{HI} are rather small.

As before, increasing the X-ray efficiency by a factor of ≈ 5 from the fiducial value has little effect on this observable. When the X-ray efficiency is further increased to account for $\approx 1/2$ of ionizations, and the reionization history is matched to the same τ_e , the $l = 3000$ patchy kSZ power is decreased by $\approx 0.5 \mu\text{K}^2$ (compare the solid black and blue dot dashed curves). On the other hand, if the UV and X-ray efficiencies are not decreased to match the same τ_e as the fiducial model, the same relative X-ray contribution ($\approx 1/2$ of ionizations) results in only a $\approx 0.2 \mu\text{K}^2$ decrease in patchy kSZ power over the fiducial model (compare the solid black and orange short dashed curves), on scales smaller than $l \approx 1000$ (≈ 60

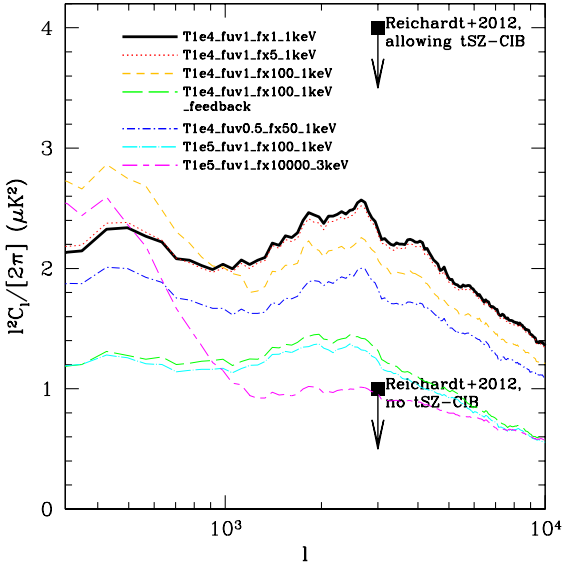


Figure 6. The kSZ power spectrum sourced from $z > 5.6$. The points denote the recent 95% C.L. on the $l = 3000$ power by Reichardt et al. (2012), assuming no tSZ-CIB correlation (*bottom point*) and allowing for a tSZ-CIB correlation (*upper point*). The points also include a conservatively-low contribution of $\approx 2\mu K^2$ from the $z < 5.6$ OV signal (e.g. Shaw et al. 2012; Mesinger et al. 2012).

Mpc)¹¹. In this case, the more uniform component resulting from the X-rays is counteracted by shifting reionization to earlier epochs. An earlier reionization increases the kSZ signal in Fig. 6 through: (i) an increase in the mean density of the IGM in the integrand of eq. 11; and (ii) a larger post-reionization (OV) component to the signal down to $z = 5.6$, the redshift cut we use.

This is illustrated in the top panel of Fig. 7, where we show the cumulative fraction of the $z > 5.6$ kSZ signal at $l = 3000$ sourced at global neutral fractions less than \bar{x}_{HI} . In the fiducial model, $\approx 20\%$ of the total $z > 5.6$ power comes from post-reionization (OV) $5.6 < z \lesssim 8$, and the other 80% comes from the epoch of reionization (patchy kSZ). When the X-ray efficiency is increased by a factor of 100, these fractions change to 30% (70%) for the OV (patchy) kSZ components. However, the shape of this cumulative density distribution (CDF) is essentially unchanged. On the other hand, as we increase T_{vir} , a larger fraction of the power is sourced from the early stages of reionization. As noted in Mesinger et al. (2012), increasing T_{vir} results in a more uniform HII bubble size, reducing the small-scale structure. In the later stages of reionization, it is the small-scale structure (the tail of the HII bubble distribution), which dominates the power on $l = 3000$ ($\approx 20\text{Mpc}$) scales. This is further evidence that using $[\Delta_{l3000}]^2$ to place limits on the end of reionization is highly model-dependent.

Understandably, T1e5_fuv1_fx10000_3keV has the largest impact on the patchy kSZ signal. In fact, it is the only one of our models which is marginally consistent with the recent aggressive SPT bounds on $[\Delta_{l3000}]^2$. From the top panel of Fig. 7, we see that 60% of the $z > 5.6$ power in the model just comes from the OV effect post-reionization, $5.6 < z \lesssim 9$. Since this model is already un-

¹¹ Behavior on larger scales is difficult to interpret due to cosmic variance in the integrand of eq. (11): $n_e \hat{\mathbf{u}} \cdot \mathbf{v}$ (Jelić et al. 2010; Jelić et al., in preparation). However, these scales are dominated by the primary anisotropies, and so are impossible to be used for the kSZ in the near future.

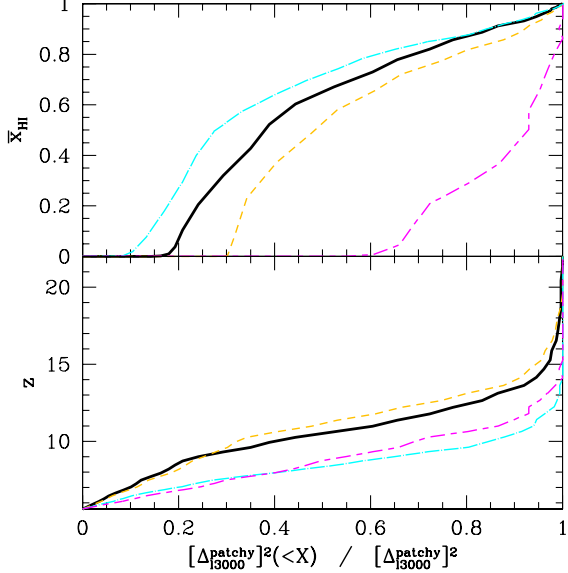


Figure 7. The cumulative fraction of the $z > 5.6$ kSZ signal at $l = 3000$ sourced by redshifts less than z (*bottom panel*) and corresponding global neutral fractions less than \bar{x}_{HI} (*top panel*). We show the same models as in Fig. 3.

realistically extreme (see the discussion in §2.3), we conclude that X-rays could not by themselves match the recent aggressive bound from SPT. *There must be a sizable contribution from the tSZ-CIB cross-correlation.*

3.4 Cosmological 21cm Signal

The most promising probe of early X-rays is probably the redshifted 21cm line from IGM neutral hydrogen. Precursor instruments like EDGES have already ruled out extremely rapid ($\Delta z \lesssim 0.06$) reionization models from the all-sky signal (Bowman & Rogers 2010). First generation interferometers, like the Low Frequency Array (LOFAR; Harker et al. 2010)¹², Murchison Wide Field Array (MWA; Tingay et al. 2012)¹³, and the Precision Array for Probing the Epoch of Re-ionization (PAPER; Parsons et al. 2010)¹⁴ are coming on-line, promising to measure the 21cm power spectrum during $7 \lesssim z \lesssim 11$. Second generation instruments, such as the Square Kilometer Array (SKA; Mellema et al. 2012)¹⁵ and the Lunar University Network for Astrophysical Research (LUNAR)¹⁶, should have the sensitivity to directly image the topology of reionization (low signal-to-noise, large-scale images might even be possible with first-generation interferometers; Zaroubi et al. 2012). In addition to reionization, *the 21cm signal is also a sensitive probe of the thermal history of the IGM pre-reionization, when early X-rays have the largest imprint* (e.g. Furlanetto 2006).

The 21cm signal is usually represented in terms of the offset of the 21cm brightness temperature from the CMB temperature, T_{γ} , along a line of sight (LOS) at observed frequency ν (c.f. Furlanetto et al. 2006):

¹² <http://www.lofar.org/>

¹³ <http://www.mwatelescope.org/>

¹⁴ <http://astro.berkeley.edu/~dbacker/eor/>

¹⁵ <http://www.skatelescope.org/>

¹⁶ <http://lunar.colorado.edu>

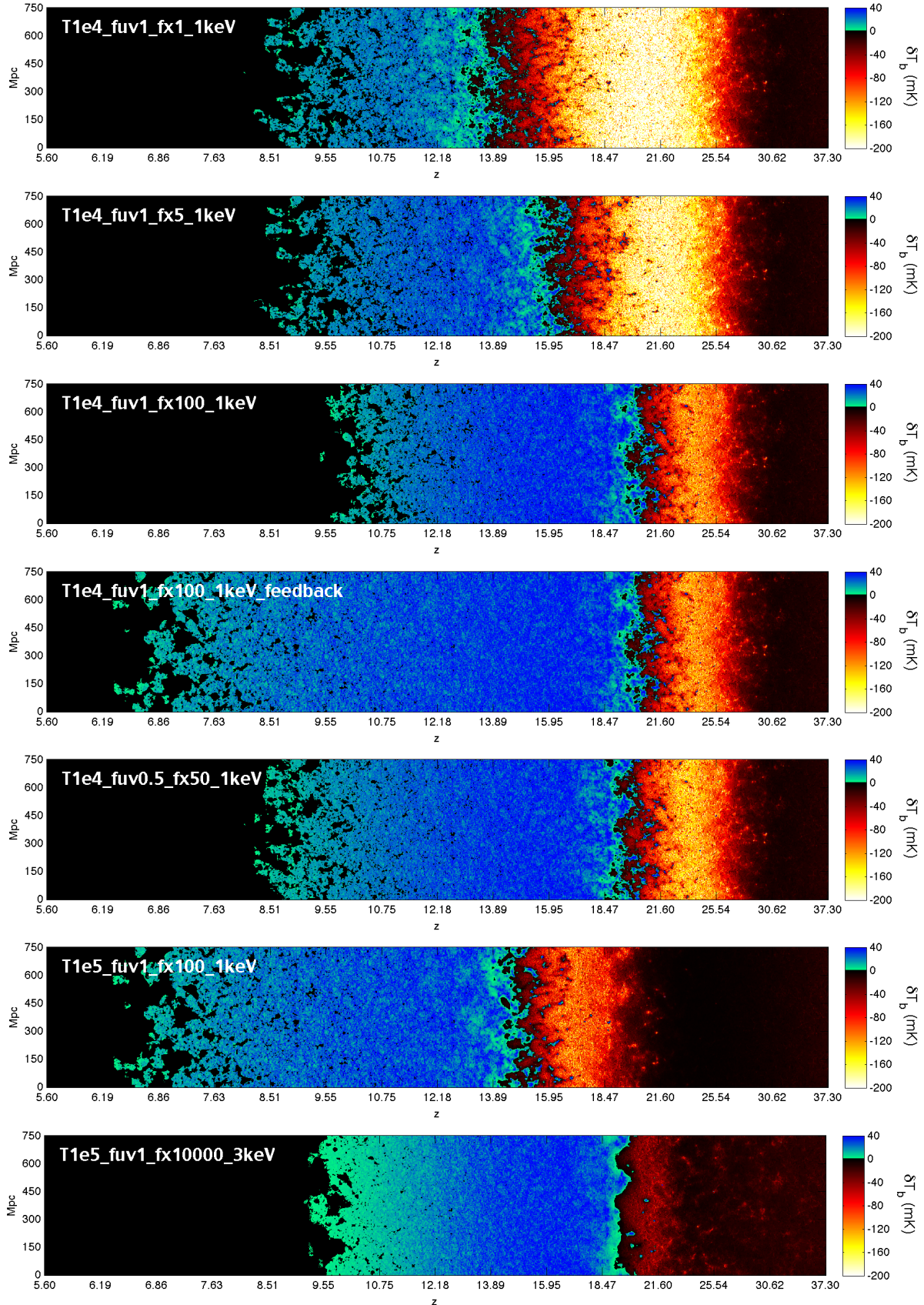


Figure 8. Slices through the predicted 21cm signal for our models. The slices show evolution with comoving distance along the light cone (x-axis). For movies of some of these models, please see http://homepage.sns.it/mesinger/21cm_Movie.html.

$$\delta T_b(\nu) = \frac{T_S - T_\gamma}{1 + z} (1 - e^{-\tau_{\nu_0}}) \approx 27x_{\text{HI}}(1 + \delta_{\text{nl}}) \left(\frac{H}{dv_r/dr + H} \right) \left(1 - \frac{T_\gamma}{T_S} \right) \times \left(\frac{1 + z}{10} \frac{0.15}{\Omega_M h^2} \right)^{1/2} \left(\frac{\Omega_b h^2}{0.023} \right) \text{mK}, \quad (12)$$

where T_S is the gas spin temperature, τ_{ν_0} is the optical depth at the 21-cm frequency ν_0 , $\delta_{\text{nl}}(\mathbf{x}, z) \equiv \rho/\bar{\rho} - 1$ is the evolved (Eulerian) density contrast, $H(z)$ is the Hubble parameter, dv_r/dr is the comoving gradient of the line of sight component of the comoving velocity, and all quantities are evaluated at redshift $z = \nu_0/\nu - 1$.

The spin temperature interpolates between the CMB temperature and the gas kinetic temperature, T_K . Since the observation uses the CMB as a backlight, a signal is only obtained if $T_S \rightarrow T_K$. This coupling is achieved through either: (i) collisions, which are effective in the IGM at high redshifts, $z \gtrsim 50$; or (ii) a Lyman alpha background [so-called Wouthuysen-Field (WF) coupling; Wouthuysen 1952; Field 1958], effective soon after the first sources turn on.

In Fig. 8, we show slices through the δT_b fields in our models. It is immediately obvious that the 21cm signal is a physics-rich probe, encoding information on various processes during and before reionization. Although the exact timing varies, all of our models show the same, fiducial sequence (c.f. Furlanetto 2006; §2.1 in McQuinn & O’Leary 2012):

(i) **Collisional coupling:** The IGM is dense at high redshifts, so the spin temperature is uniformly collisionally coupled to the gas kinetic temperature, $T_K = T_S \lesssim T_\gamma$. Following thermal decoupling from the CMB ($z \lesssim 300$), the IGM cools adiabatically as $T_K \propto (1 + z)^2$, faster than the CMB, $T_\gamma \propto (1 + z)$. Thus δT_b is negative. This epoch, serving as a clean probe of the matter power spectrum at $z \gtrsim 100$, is not shown in Fig. 8.

(ii) **Collisional decoupling:** The IGM becomes less dense as the Universe expands. The spin temperature starts to decouple from the kinetic temperature, and begins to approach the CMB temperature again, $T_K < T_S \lesssim T_\gamma$. Thus δT_b starts rising towards zero. Decoupling from T_K occurs as a function of the local gas density, with underdense regions decoupling first. Eventually (by $z \sim 25$), all of the IGM is decoupled and there is little or no signal. This epoch corresponds to the black region in the far right of the panels in Fig. 8.

(iii) **WF coupling (i.e. Ly α pumping):** The first astrophysical sources turn on, and begin coupling T_S and T_K , this time through the WF effect. δT_b becomes more negative, reaching values as low as $\delta T_b \sim 100\text{--}200$ (depending on the offset of the WF and X-ray heating epochs). This epoch corresponds to the black \rightarrow yellow transition¹⁷ in the panels of Fig. 8.

(iv) **X-ray heating:** X-rays heat the IGM, with the spin temperature now coupled to the gas temperature, $T_K = T_S$. As the gas temperature surpasses T_γ , the 21cm signal changes from absorption to emission, becoming insensitive to the actual value of T_S

¹⁷ The Lyman α background has two main contributors: (i) X-ray excitation of HI; and (ii) direct stellar emission of photons between Ly α and the Lyman limit. In general, we find that either (ii) dominates, or the two are comparable. However in our extreme model (see the bottom panel of Fig. 8), the direct excitation by X-rays is clearly driving the WF coupling, imprinting a very interesting spatial structure to the epoch.

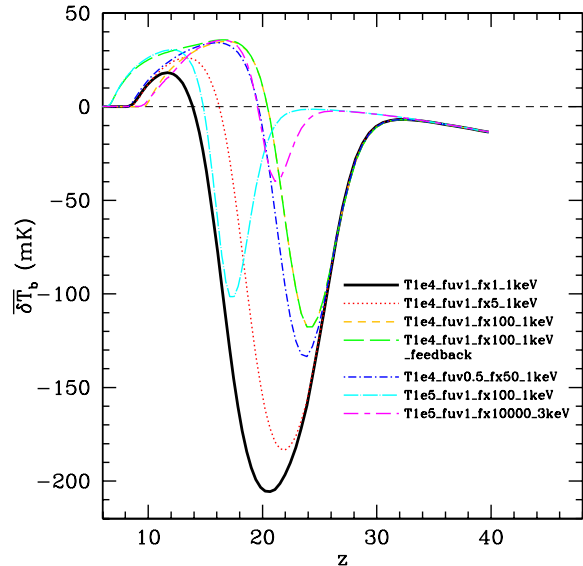


Figure 9. Redshift evolution of the average 21cm brightness temperature offset from the CMB.

(see eq. 12). This epoch corresponds to the yellow \rightarrow blue transition in the panels of Fig. 8.

(v) **Reionization:** the IGM becomes ionized, a process which is inside-out on large scales. The signal again approaches zero. This epoch corresponds to the blue \rightarrow black transition in the panels of Fig. 8.

These stages can be seen in more quantitative detail in Fig. 9, where we plot the corresponding evolution of the average δT_b . This figure clearly shows the emission peak and absorption trough. The position and height/depth of the mean signal depends on the timing of the astrophysical milestones discussed above¹⁸. The photon production rates in our models trace the evolution of the collapse fraction, f_{coll} . Hence, if smaller dark matter (DM) halos host the first sources, then WF coupling, X-ray heating and reionization will occur earlier, and more gradually¹⁹.

All other things being equal, the stronger the X-ray efficiency of the early sources, the shallower the δT_b absorption trough. This is due to two reasons: (i) X-ray heating can begin before WF coupling is complete with $T_S > T_K$; (ii) the ratio T_γ/T_K evolves roughly as $\propto (1 + z)^{-1}$ prior to heating, so earlier X-ray heating results in a smaller δT_b contrast even if $T_S \approx T_K$.

Following X-ray heating, the $(1 - T_\gamma/T_S)$ term in eq. (12) goes to unity and the IGM is seen in emission against the CMB. If there is subsequently a delay before the onset of reionization, then only the cosmological terms in eq. (12) are not unity, and the mean signal decreases as $\delta \bar{T}_b \propto \sqrt{1 + z}$. Such an epoch would facilitate a clean measurement of the matter power spectrum at lower, more accessible redshifts than the Dark Ages. We see in Fig. 9 that this would occur if reionization was driven by more massive

¹⁸ Our fiducial model has a deeper $\delta \bar{T}_b$ absorption trough and a lower emission peak than some previous estimates based on Furlanetto (2006), due to our choice of a lower fiducial X-ray efficiency as discussed in §2.3. A lower X-ray efficiency results in a wider WF coupling \rightarrow X-ray heating transition, and a narrower X-ray heating \rightarrow reionization transition.

¹⁹ Even more gradual heating can result in some DM annihilation models, since the heating is driven by the collapse fraction in $\gtrsim M_\odot$ DM halos (Valdés et al. 2012).

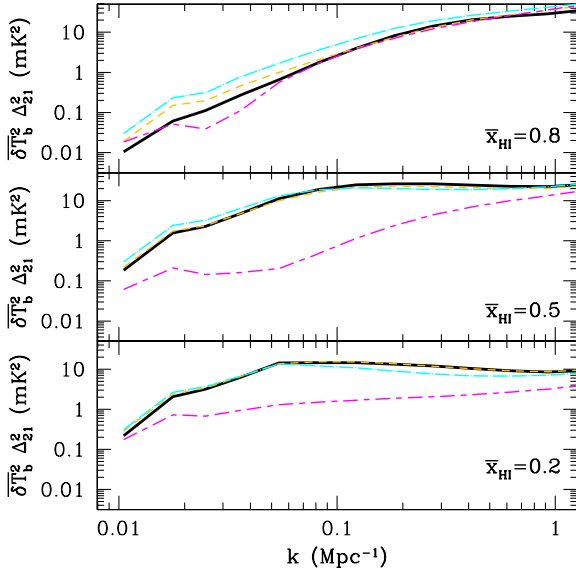


Figure 10. 21cm power spectra from the same models as in Fig. 3, shown at $\bar{x}_{\text{HI}} = 0.8, 0.5, 0.2$ (top to bottom).

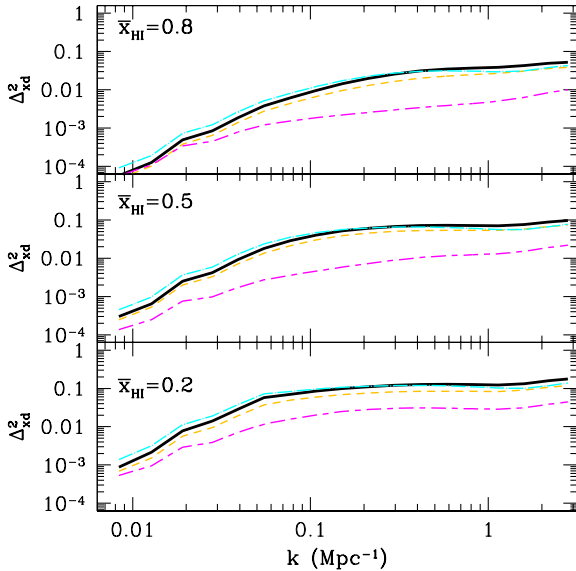


Figure 11. Ionization-density cross power spectrum for the same models as in Fig. 3, shown at $\bar{x}_{\text{HI}} = 0.8, 0.5, 0.2$ (top to bottom).

sources than those driving X-ray heating, such as would be the case with strong thermal feedback (T1e4_fuv1_fx100_1keV_feedback; see also the fourth panel in Fig. 8).

In Fig. 10, we show the 21cm power spectra from the same models and epochs shown in Fig. 4. Some of the same qualitative trends as noted in Fig. 4 can also be seen in Fig. 10; however the differences between the models are smaller. This can be understood if we decompose the 21cm power spectrum (post-heating) to first-order:

$$\Delta_{21}^2 = \bar{T}_b^2 [\Delta_{xx}^2 - 2\bar{x}_{\text{HI}}\Delta_{xd}^2 + \bar{x}_{\text{HI}}^2\Delta_{dd}^2], \quad (13)$$

where \bar{T}_b is the average brightness temperature in regions with $\bar{x}_{\text{HI}} = 1$, and P is the power spectrum of the ionization (X) and density (D) fields. As we saw in §3.2, the more-uniform X-ray component decreases Δ_{xx}^2 on small scales. However, this mild decrease is compensated by a decrease in the cross-correlation term,

Δ_{xd}^2 (shown in Fig. 11), which contributes negatively to the 21cm power. The impact of the cross term is most evident in the early stages of reionization, where the fiducial model (black curve) has a factor of $\lesssim 2$ –3 less 21cm power at $k \lesssim 0.1 \text{ Mpc}^{-1}$ than T1e4_fuv1_fx100_1keV (orange curve).

In Fig. 12, we focus on the evolution of the $k = 0.1 \text{ Mpc}^{-1}$ mode, likely to lie in the middle of the decade of k -modes probed by the first generation interferometers (e.g. Furlanetto et al. 2009a; Lidz et al. 2008; Chapman et al. 2012). The evolution of our fiducial model agrees very well with the numerical simulations of Baek et al. (2010) (see the solid curves of the S6 model in their Fig. 6; this model has a similar X-ray efficiency as our fiducial model), but with their evolution shifted to later times (with their resolution they were unable to account for the large majority of atomically-cooled galaxies).

As discussed in previous works (Pritchard & Furlanetto 2007; Baek et al. 2010; Mesinger et al. 2011), the evolution of the $k = 0.1 \text{ Mpc}^{-1}$ large-scale power has three peaks, corresponding to the epochs of Ly α pumping, X-ray heating and reionization. The earlier peaks (especially the X-ray heating one) are larger, due to the larger contrast available in the 21cm absorption regime. The position and width of these peaks scale with the model parameters. A higher T_{vir} results in delayed and more rapid transitions, tracing the growth of the exponential, high-mass tail of the halo mass function. Increasing the X-ray efficiency mainly shifts the X-ray heating peak to earlier epochs. If X-ray heating occurs early enough (e.g. $fx \gtrsim 10$), it overlaps with the Ly α pumping epoch, decreasing the associated peak in power. Our extreme run, T1e5_fuv1_fx10000_3keV, generally has less power on $k = 0.1 \text{ Mpc}^{-1}$ scales throughout cosmic time, with the X-ray heating and WF coupling epochs overlapping significantly. The hard X-rays driving both epochs create radiation fields with little small-scale structure, while fluctuations in both Ly α and gas temperature source the large-scale power; this results in a negative slope at $k = 0.1 \text{ Mpc}^{-1}$ during X-ray heating (bottom panel).

Zooming-in on the reionization epoch, in the right panel of Fig. 12 we plot the same quantities as a function of \bar{x}_{HI} . In the advanced stages of reionization, our results are in excellent agreement with those in Lidz et al. (2008), who only considered reionization under the commonly-used assumption of $T_S \gg T_\gamma$ (see their Fig. 2). Lidz et al. (2008) note that the inside-out nature of reionization causes a drop in large-scale 21cm contrast at early times ($\bar{x}_{\text{HI}} \gtrsim 0.9$), before the growth of ionization structures pushes the power back up. Stated differently in terms of eq. (13), the 21cm power before reionization (and assuming $T_S \gg T_\gamma$) traces the matter power spectrum, Δ_{dd}^2 . In the early stages when HII regions are small, the large-scale power drops due to the increase in the cross-correlation term, Δ_{xd}^2 , which contributes negatively. Then at $\bar{x}_{\text{HI}} \lesssim 0.9$, the HII bubbles grow, dominating the 21cm power through the Δ_{xx}^2 term. The $k = 0.1 \text{ Mpc}^{-1}$ 21cm power subsequently peaks at $\bar{x}_{\text{HI}} \approx 0.5$ (Lidz et al. 2008; Friedrich et al. 2011), with weak scale dependence (i.e. roughly zero slope; Zahn et al. 2011; Mesinger et al. 2011). These trends are evident in the right panel of Fig. 12.

Including X-rays impacts this scenario in two main ways. Firstly, the long mean free path of X-rays, combined with their lower ionization efficiency in regions with a higher ionized fraction, results in the uniform, partially-ionized ‘haze’, seen most clearly in the bottom panel of Fig. 1. Therefore, models with a large fraction of X-ray ionizations have a weaker and slower growth of the Δ_{xd}^2 and Δ_{xx}^2 terms. This results in a more extended initial stage of reionization (with the large-scale 21cm power falling as Δ_{xd}^2 in-

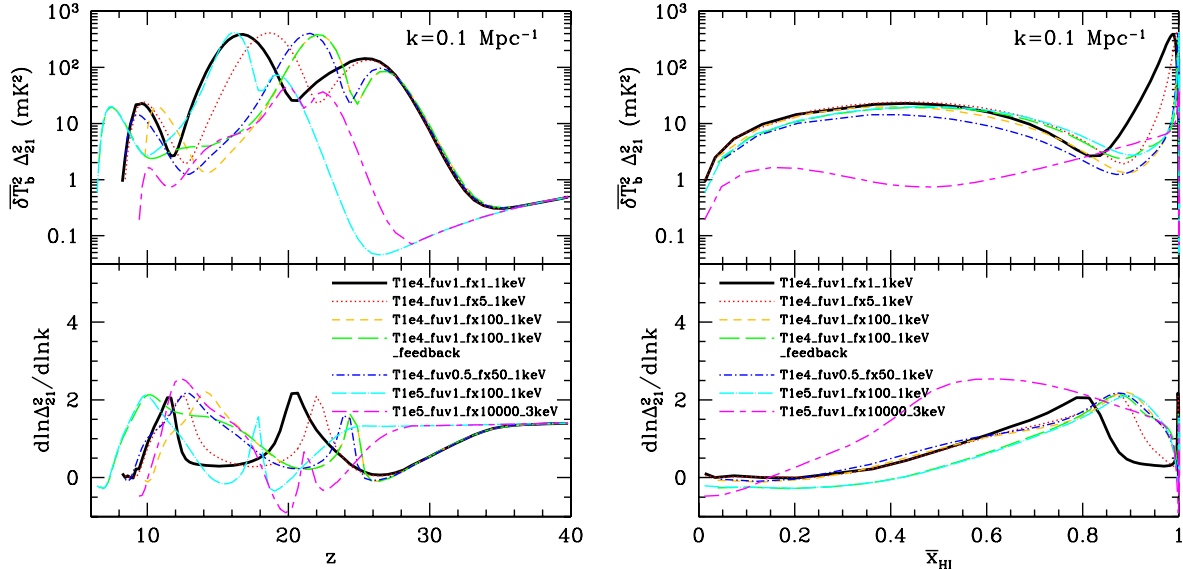


Figure 12. Evolution of the 21cm power (top panels) and its slope (bottom panels) at $k = 0.1 \text{ Mpc}^{-1}$. Evolution is shown against redshift on the left, and against \bar{x}_{HI} on the right.

creases, before it becomes dominated by the ionization structure, i.e. Δ_{xx}^2). However, this effect is only really evident in the extreme T1e5_fuv1_fx10000_3keV model, where the $k = 0.1 \text{ Mpc}^{-1}$ power continues to fall until $\bar{x}_{\text{HI}} \approx 0.5$, roughly the epoch when $\Delta_{\text{xx}}^2 \sim \Delta_{\text{xd}}^2$ (compare Figures 11 and 4). In the other models UV + softer X-ray photons drive the usual evolution of Δ_{21}^2 described above, with the difference in power between the models being less than a factor of 2, even when X-rays contribute $\approx 1/2$ of the ionizations.

Secondly, and more importantly, we see that *in realistic X-ray models the assumption of $T_S \gg T_\gamma$ is not valid in the early stages of reionization*. Instead, the reionization and X-ray heating epochs overlap in virtually all of our models, resulting in a strong, scale-free drop in power at $\bar{x}_{\text{HI}} \gtrsim 0.8$ –0.9. This overlap is most notable in our fiducial model, which has the weakest X-ray heating. Note that the peak of the mean brightness temperature, $\delta \bar{T}_b$, in this model occurs at $z \approx 12$, when reionization was already well underway, $\bar{x}_{\text{HI}} \approx 0.8$.

4 CONCLUSIONS

Recent interest has focused on X-rays as a possibly significant contributor to cosmic reionization (e.g. Haiman 2011; Mirabel et al. 2011; Fontanot et al. 2012). X-ray driven reionization would be fundamentally different from a UV driven one. In particular, reionization could be more extended with a more uniform morphology. In this work, we model the observational signatures of X-rays in the early Universe, attempting to provide an intuitive framework for interpreting upcoming observations.

We use the public code, 21CMFAST, to generate seven different models of reionization and pre-heating. Our simulations are 750 Mpc on a side (currently unachievable by standard RT approaches hoping to capture the contribution from the dominant galaxy population), and span the redshift range $5.6 < z < 40$. We vary astrophysical parameters, looking for general trends and physical insight. In addition to studying the timing and morphology of reionization, we also predict the kSZ and 21cm signatures in our models.

We find that by increasing the X-ray contribution, reioniza-

tion occurs earlier, has less small-scale structure, and develops a partially-ionized homogeneous ‘haze’. However, when compared at the same \bar{x}_{HI} , the impact is modest. Namely, X-rays yield fewer small HII regions, with the IGM between HII regions being partially ionized. Larger HII regions are less affected, since these host the first, highly-biased X-ray sources. In these regions the X-rays themselves pre-ionized a large fraction of the HI, making it easier for the UV photons to finish the job. Specifically, we find that models with a significant (tens of percent) contribution of X-rays to reionization exhibit: (i) a lack of fully neutral regions, and (ii) a suppression of small-scale ($k \gtrsim 0.1 \text{ Mpc}^{-1}$) ionization power by a factor of $\lesssim 2$. These changes in the reionization morphology cannot be countered by having more biased sources (i.e. a higher T_{vir}), and are therefore a robust indicator of an X-ray contribution to reionization.

The suppression of small-scale ionization structure by X-rays also results in a smaller kSZ signal at $l = 3000$. In particular, if X-rays contribute $\approx 1/2$ of ionizations, the patchy kSZ power is decreased by $\approx 0.5 \mu\text{K}^2$ with respect to a UV-only model having the same reionization history. The shape of the $10^3 < l < 10^4$ power spectrum remains largely unaffected. The kSZ signal is reduced strongly enough to be marginally consistent with the recent aggressive SPT constraint (Reichardt et al. 2012), only if X-rays fully reionize the Universe. Since this model is already unrealistically extreme (see the discussion in §2.3), it is highly unlikely that X-ray reionization can by itself match this bound, which assumes no tSZ-CIB cross-correlation. We therefore conclude that there must be a sizable contribution from the tSZ-CIB cross-correlation.

In general, X-rays have a small impact on the 21cm signal during the advanced stages of reionization ($\bar{x}_{\text{HI}} \lesssim 0.8$), when compared at the same \bar{x}_{HI} . The difference in 21cm power is less than a factor of ≈ 2 , even when X-rays contribute $\approx 1/2$ of the ionizations. The impact of X-rays on 21cm power is less than that on morphology, since the suppression of the ionization power is compensated by a decrease in the density-ionization cross-correlation (which contributes negatively to the 21cm power). On the other hand, if harder X-rays complete reionization (our ‘extreme’ model), the 21cm power could be lower by more than an order of magnitude

in the later half of reionization, and there would be a local minimum in the evolution of large-scale power at $\bar{x}_{\text{HI}} \approx 0.5$ (see top right panel of Fig. 12).

The situation is different in the early stages of reionization ($\bar{x}_{\text{HI}} \gtrsim 0.8$), as well as the pre-reionization epochs. During the pre-reionization epochs, X-rays govern the timing and duration of IGM heating. The large-scale ($k \approx 0.1 \text{ Mpc}^{-1}$) 21cm power shows three maxima, corresponding to Ly α pumping, X-ray heating and reionization, with the X-ray heating one being the highest of the three. During the early stages of reionization ($\bar{x}_{\text{HI}} \gtrsim 0.8$), X-rays can also have a large impact on the 21cm power spectrum. This is primarily due to the overlap of the X-ray heating epoch and the early stages of reionization. The overlap is strongest in our fiducial model, which has the weakest X-ray emissivity. In particular, this overlap can lead to $\gtrsim 10$ times more power at $k \approx 0.1 \text{ Mpc}^{-1}$ than predicted with the commonly-used simplifying assumption of $T_S \gg T_\gamma$ (e.g. Mesinger & Furlanetto 2007; Lidz et al. 2008).

On the other hand, if thermal feedback was very efficient, the early X-ray emitting galaxies would self-sterilize by increasing the Jeans mass in the IGM, and reionization would be driven by more massive, later appearing sources (e.g. Ricotti & Ostriker 2004). Such a scenario would result in an extended period after the completion of X-ray heating and before the beginning of reionization. In this interim period, the 21cm line would be seen in emission, and would offer a clean probe of the matter power spectrum. This probe of cosmology occurs at much lower redshifts (making it easier to observe) than the commonly-implored Dark Ages at $z \gtrsim 40$ (e.g. Furlanetto et al. 2009b).

In closing, we enumerate some quantitative observational signatures which can be used to constrain the first generations of X-ray sources:

- (i) an X-ray contribution to reionization of \gtrsim tens of percent would result in a lack of (almost) fully-neutral ($x_{\text{HI}} \gtrsim 0.9$) regions which are \sim few cMpc in scale, during the last half of reionization;
- (ii) a 21cm power spectrum tracing the matter power spectrum in emission can indicate strong thermal feedback from early X-rays;
- (iii) if reionization is driven by ~ 1 keV X-rays, we expect the large-scale ($k \approx 0.1 \text{ Mpc}^{-1}$) 21cm power to fall until around $\bar{x}_{\text{HI}} \approx 0.5$, then rise again until $\bar{x}_{\text{HI}} \approx 0.2$, thereby creating a local minimum at $\bar{x}_{\text{HI}} \approx 0.5$ where standard models instead predict a local maximum (see the top panel of Fig. 12).
- (iv) if high- z galaxies are more efficient at producing X-rays than local ones, the rise in 21cm power associated with X-ray heating would occur earlier, at $\bar{x}_{\text{HI}} \gtrsim 0.9$.

We thank Matthew McQuinn for comments on a draft version of this paper.

REFERENCES

Abel T., Bryan G. L., Norman M. L., 2002, *Science*, 295, 93

Ahn K., Iliev I. T., Shapiro P. R., Mellema G., Koda J., Mao Y., 2012, *ApJ*, 756, L16

Alvarez M. A., Abel T., 2012, *ApJ*, 747, 126

Baek S., Semelin B., Di Matteo P., Revaz Y., Combes F., 2010, *A&A*, 523, A4

Barkana R., Loeb A., 2005, *ApJ*, 626, 1

Barkana R., Loeb A., 2008, *MNRAS*, 384, 1069

Basu-Zych A. R., et al., 2012, ArXiv e-prints:1210.3357

Bolton J. S., Haehnelt M. G., 2007, *MNRAS*, 382, 325

Bolton J. S., Haehnelt M. G., Warren S. J., Hewett P. C., Mortlock D. J., Venemans B. P., McMahon R. G., Simpson C., 2011, *MNRAS*, 416, L70

Bond J. R., Cole S., Efstathiou G., Kaiser N., 1991, *ApJ*, 379, 440

Bouwens R. J., Illingworth G. D., Franx M., Ford H., 2008, *ApJ*, 686, 230

Bowman J. D., Rogers A. E. E., 2010, *Nature*, 468, 796

Bromm V., Coppi P. S., Larson R. B., 2002, *ApJ*, 564, 23

Cappelluti N., et al., 2012, ArXiv e-prints:1210.5302

Cen R., 2006, *ApJ*, 648, 47

Chapman E., et al., 2012, *MNRAS*, 423, 2518

Choudhury T. R., Haehnelt M. G., Regan J., 2009, *MNRAS*, 394, 960

Cowie L. L., Barger A. J., Hasinger G., 2012, *ApJ*, 748, 50

Crociani D., Mesinger A., Moscardini L., Furlanetto S., 2011, *MNRAS*, 411, 289

Crowther P. A., Barnard R., Carpano S., Clark J. S., Dhillon V. S., Pollock A. M. T., 2010, *MNRAS*, 403, L41

Dijkstra M., Haiman Z., Loeb A., 2004, *ApJ*, 613, 646

Dijkstra M., Mesinger A., Wyithe J. S. B., 2011, *MNRAS*, 414, 2139

Fan X., et al., 2001, *AJ*, 122, 2833

Ferrara A., Loeb A., 2012, ArXiv e-prints:1209.2123

Field G. B., 1958, *Proceedings of the Institute of Radio Engineers*, 46, 240

Finlator K., Davé R., Özel F., 2011, ArXiv e-prints:1106.4321

Fontanot F., Cristiani S., Vanzella E., 2012, *MNRAS*, 425, 1413

Friedrich M. M., Mellema G., Alvarez M. A., Shapiro P. R., Iliev I. T., 2011, *MNRAS*, 413, 1353

Furlanetto S. R., 2006, *MNRAS*, 371, 867

Furlanetto S. R., et al., 2009a, in astro2010: The Astronomy and Astrophysics Decadal Survey Vol. 2010 of ArXiv Astrophysics e-prints:0902.3011, Astrophysics from the Highly-Redshifted 21 cm Line. pp 83–+

Furlanetto S. R., et al., 2009b, in astro2010: The Astronomy and Astrophysics Decadal Survey Vol. 2010 of ArXiv Astrophysics e-prints:0902.3259, Cosmology from the Highly-Redshifted 21 cm Line. pp 82–+

Furlanetto S. R., Mesinger A., 2009, *MNRAS*, 394, 1667

Furlanetto S. R., Oh S. P., 2005, *MNRAS*, 363, 1031

Furlanetto S. R., Oh S. P., Briggs F. H., 2006, *Physics Reports*, 433, 181

Furlanetto S. R., Stoever S. J., 2010, *MNRAS*, 404, 1869

Furlanetto S. R., Zaldarriaga M., Hernquist L., 2004, *ApJ*, 613, 1

Gilfanov M., Grimm H.-J., Sunyaev R., 2004, *MNRAS*, 347, L57

Gnedin N. Y., 2000, *ApJ*, 542, 535

Gnedin N. Y., Kravtsov A. V., Chen H.-W., 2008, *ApJ*, 672, 765

Greiner J., et al., 2009, *ApJ*, 693, 1610

Gruzinov A., Hu W., 1998, *ApJ*, 508, 435

Haiman Z., 2011, *Nature*, 472, 47

Haiman Z., Abel T., Rees M. J., 2000, *ApJ*, 534, 11

Haiman Z., Bryan G. L., 2006, *ApJ*, 650, 7

Haiman Z., Thoul A. A., Loeb A., 1996, *ApJ*, 464, 523

Harker G., et al., 2010, *MNRAS*, 405, 2492

Hickox R. C., Markevitch M., 2007, *ApJ*, 661, L117

Jelić V., et al., 2010, *MNRAS*, 402, 2279

Kaaret P., Schmitt J., Gorski M., 2011, *ApJ*, 741, 10

Knox L., Scoccimarro R., Dodelson S., 1998, *Physical Review Letters*, 81, 2004

Komatsu E., et al., 2011, *ApJS*, 192, 18

Kuhlen M., Faucher-Giguere C.-A., 2012, ArXiv e-prints: 1201.0757

Kuhlen M., Madau P., 2005, *MNRAS*, 363, 1069

Labbe I., et al., 2010, *ApJ*, 708, L26

Lacey C., Cole S., 1993, *MNRAS*, 262, 627

Lehmer B. D., Alexander D. M., Bauer F. E., Brandt W. N., Goulding A. D., Jenkins L. P., Ptak A., Roberts T. P., 2010, *ApJ*, 724, 559

Lidz A., McQuinn M., Zaldarriaga M., Hernquist L., Dutta S., 2007, *ApJ*, 670, 39

Lidz A., Zahn O., McQuinn M., Zaldarriaga M., Hernquist L., 2008, *ApJ*, 680, 962

Lutovinov A., Revnivtsev M., Gilfanov M., Shtykovskiy P., Molkov S., Sunyaev R., 2005, *A&A*, 444, 821

Ma C., Fry J. N., 2002, *Physical Review Letters*, 88, 211301

Mack K. J., Wyithe J. S. B., 2011, *ArXiv e-prints*:1101.5431

Madau P., Haardt F., Rees M. J., 1999, *ApJ*, 514, 648

Madau P., Rees M. J., Volonteri M., Haardt F., Oh S. P., 2004, *ApJ*, 604, 484

McGreer I. D., Mesinger A., Fan X., 2011, *MNRAS*, 415, 3237

McQuinn M., 2012, *ArXiv e-prints*:1206.1335

McQuinn M., Lidz A., Zahn O., Dutta S., Hernquist L., Zaldarriaga M., 2007, *MNRAS*, 377, 1043

McQuinn M., Oh S. P., Faucher-Giguère C.-A., 2011, *ApJ*, 743, 82

McQuinn M., O’Leary R. M., 2012, *ArXiv e-prints*:1204.1345

Mellema G., et al., 2012, *ArXiv e-prints*

Mesinger A., Bryan G. L., Haiman Z., 2006, *ApJ*, 648, 835

Mesinger A., Dijkstra M., 2008, *MNRAS*, 390, 1071

Mesinger A., Furlanetto S., 2007, *ApJ*, 669, 663

Mesinger A., Furlanetto S., Cen R., 2011, *MNRAS*, 411, 955

Mesinger A., McQuinn M., Spergel D. N., 2012, *MNRAS*, 422, 1403

Mineo S., Gilfanov M., Sunyaev R., 2012, *MNRAS*, 419, 2095

Mirabel I. F., Dijkstra M., Laurent P., Loeb A., Pritchard J. R., 2011, *A&A*, 528, A149

Miralda-Escudé J., 2003, *ApJ*, 597, 66

Mitra S., Ferrara A., Choudhury T. R., 2012, *ArXiv e-prints*:1207.3803

Okamoto T., Gao L., Theuns T., 2008, *MNRAS*, 390, 920

O’Leary R. M., McQuinn M., 2012, *ArXiv e-prints*:1204.1344

Ostriker J. P., Vishniac E. T., 1986, *ApJ*, 306, L51

Paardekooper J.-P., Pelupessy F. I., Altay G., Kruip C. J. H., 2011, *A&A*, 530, A87+

Parsons A. R., et al., 2010, *AJ*, 139, 1468

Pawlak A. H., Milosavljevic M., Bromm V., 2012, *ArXiv e-prints*:1208.3698

Pawlak A. H., Schaye J., 2009, *MNRAS*, 396, L46

Pentericci L., et al., 2011, *ApJ*, 743, 132

Persic M., Rephaeli Y., 2007, *A&A*, 463, 481

Persic M., Rephaeli Y., Braito V., Cappi M., Della Ceca R., Franceschini A., Gruber D. E., 2004, *A&A*, 419, 849

Pritchard J. R., Furlanetto S. R., 2007, *MNRAS*, 376, 1680

Ranalli P., Comastri A., Setti G., 2003, *A&A*, 399, 39

Reichardt C. L., et al., 2012, *ApJ*, 755, 70

Ricotti M., Gnedin N. Y., Shull J. M., 2001, *ApJ*, 560, 580

Ricotti M., Gnedin N. Y., Shull J. M., 2002, *ApJ*, 575, 49

Ricotti M., Ostriker J. P., 2004, *MNRAS*, 352, 547

Salvaterra R., Ferrara A., Dayal P., 2011, *MNRAS*, 414, 847

Salvaterra R., Haardt F., Volonteri M., 2007, *MNRAS*, 374, 761

Santos M. G., Amblard A., Pritchard J., Trac H., Cen R., Cooray A., 2008, *ApJ*, 689, 1

Schroeder J., Mesinger A., Haiman Z., 2012, *ArXiv e-prints*:1204.2838

Shapiro P. R., Giroux M. L., Babul A., 1994, *ApJ*, 427, 25

Shaw L. D., Rudd D. H., Nagai D., 2012, *ApJ*, 756, 15

Shull J. M., van Steenberg M. E., 1985, *ApJ*, 298, 268

Songaila A., Cowie L. L., 2010, *ApJ*, 721, 1448

Springel V., Hernquist L., 2003, *MNRAS*, 339, 312

Srbinovsky J. A., Wyithe J. S. B., 2007, *MNRAS*, 374, 627

Stacy A., Greif T. H., Bromm V., 2010, *MNRAS*, 403, 45

Sunyaev R. A., Zeldovich I. B., 1980, *MNRAS*, 190, 413

Thoul A. A., Weinberg D. H., 1996, *ApJ*, 465, 608

Tingay S. J., et al., 2012, *ArXiv e-prints*

Totani T., Kawai N., Kosugi G., Aoki K., Yamada T., Iye M., Ohta K., Hattori T., 2006, *PASJ*, 58, 485

Tozzi P., et al., 2006, *A&A*, 451, 457

Trac H., Cen R., 2007, *ApJ*, 671, 1

Tseliakhovich D., Hirata C., 2010, *PRD*, 82, 083520

Turk M. J., Abel T., O’Shea B., 2009, *Science*, 325, 601

Valdés M., Evoli C., Ferrara A., 2010, *MNRAS*, 404, 1569

Valdés M., Evoli C., Mesinger A., Ferrara A., Yoshida N., 2012, *ArXiv e-prints*:1209.2120

Visbal E., Loeb A., 2011, *ArXiv e-prints*:1109.5722

Vishniac E. T., 1987, *ApJ*, 322, 597

Volonteri M., Gnedin N. Y., 2009, *ApJ*, 703, 2113

Warszawski L., Geil P. M., Wyithe J. S. B., 2009, *MNRAS*, 396, 1106

Willott C. J., et al., 2010, *AJ*, 139, 906

Wise J. H., Cen R., 2009, *ApJ*, 693, 984

Wouthuysen S. A., 1952, *AJ*, 57, 31

Xue Y. Q., et al., 2011, *ApJS*, 195, 10

Zahn O., Mesinger A., McQuinn M., Trac H., Cen R., Hernquist L. E., 2011, *MNRAS*, 414, 727

Zaroubi S., et al., 2012, *ArXiv e-prints*:1205.3449